

Numerical Simulation of Reinforced Concrete Shear Walls Using Force-Based Fiber Element Method

MUHAMMET KARATON (✉ mkaraton@firat.edu.tr)

Firat Univ. Engineering Faculty

Ömer Faruk Osmanlı

Firat Üniversitesi: Firat Üniversitesi

Mehmet Eren GÜLŞAN

Gaziantep University: Gaziantep Üniversitesi

Research Article

Keywords: Shear wall, Fiber element, Force-based, Damping types, Damping ratio and Seismic loads.

Posted Date: March 17th, 2021

DOI: <https://doi.org/10.21203/rs.3.rs-296727/v1>

License: © ⓘ This work is licensed under a Creative Commons Attribution 4.0 International License.

[Read Full License](#)

Numerical Simulation of Reinforced Concrete Shear Walls Using Force-Based Fiber Element Method

Muhammet Karaton^{1a}, Ömer Faruk Osmanlı^{1b}, Mehmet Eren Gülşan^{2c}

¹Department of Civil Engineering, Fırat University, Elazığ, Turkey.

²Department of Civil Engineering, Gaziantep University, Gaziantep, Turkey.

^a e-mail: mkaraton@firat.edu.tr ORCID: 0000-0002-1498-4659

^b e-mail: ofosmanli@firat.edu.tr ORCID: 0000-0002-9799-3103

^c e-mail: gulsan@gantep.edu.tr ORCID: 0000-0002-8991-0363

Corresponding Author, Email: mkaraton@gantep.edu.tr

ABSTRACT

Reinforced concrete shear walls are the structural elements that considerably increase the seismic performance of buildings. Fiber elements and fiber-spring elements are used for the modeling of the inelastic behavior of these elements. The Fiber Element Method provides a certain amount of accuracy for the modeling of reinforced concrete shear walls. However, the studies related to this method are still in progress.

In this study, the efficiency of the force-based Fiber Element Method is investigated for different damping ratios and different damping types that used in the structural damping for reinforced concrete shear wall structures. Two shear wall structures that subjected to seismic loads are used for the comparison of numerical analysis and experimental results. The comparisons are achieved according to the absolute maximum values of the overturning moment, the base shear force, and the roof displacement. Rayleigh damping and stiffness-proportional damping types for the damping ratios that vary between 2-3% provide better results than mass-proportional damping. Additionally, the optimum number of fiber element for Rayleigh and stiffness-proportional damping types is determined for the optimum damping ratio that provides minimum differences between numerical analysis and experimental results. For these damping types, when the length of a fiber is smaller than 3% of the longitudinal length of the shear wall at the optimum damping ratios, the roof displacement differences between numerical analysis and experimental results are less than 2.5%.

Key Words: Shear wall, Fiber element, Force-based, Damping types, Damping ratio and Seismic loads.

1. Introduction

Shear walls are the structural elements that considerably enhance the lateral load capacity of the reinforced concrete (RC) structures subjected to the earthquake. There are many experimental studies to investigate the seismic behavior of these elements in the literature (Peterman et al., 2016; Shen et al., 2017; Huang et al., 2018; Wang et al., 2018; Rong et al., 2020). On the other hand, the numerical simulation of these elements is an essential researching subject for assessing the nonlinear behavior of the structures. RC shear walls are simulated by using several modeling approaches (Dashti et al., 2017; Nikolić et al., 2017; Feng et al., 2018; Zhang et al., 2020). In the most accepted numerical modeling approach, beam-column elements are utilized with nonlinear axial and rotational springs. The springs were positioned in the vertical direction of the wall center. In spite of the modification of beam-column elements conducted by using multiple springs, the model is inadequate for the modeling of shear wall behavior. The inadequacies are resulted from ignoring the interaction between the shear wall with frame elements and the neutral axis variation in wall cross-section. Three-Vertical-Line-Element Model (TVLEM) and Multiple-Vertical-Line-Element Model (MVLEM) were developed depending on the beam-column element model. In these models, the vertical line elements that containing nonlinear springs to be at the top and bottom of the wall are attached to the rigid beams (Orakcal et al. 2004). Based on the MVLEM, a macroscopic fiber model was developed to simulate the nonlinear behavior of the reinforced concrete shear wall using a series of uniaxial elements by Orakcal et al. (2004). In this model, the axial stiffness of the exterior columns is represented with at least two boundary elements. The flexural and axial stiffness of the interior panel are simulated with a minimum of two central elements. The number of uniaxial elements (macro fibers) can be enhanced for a more refined definition of the section.

The distributed plastic hinge model adopted in most design codes is commonly used to model the nonlinear behavior of RC structural elements. In this model, steel reinforcement and concrete portions in the cross-section of each structural element are simulated by fiber elements. The nonlinear response of the structural element is calculated by weighted integration of the behavior of the cross-sections by considering the material nonlinearity. The element deformations and the element forces are determined by convenient interpolation functions in the global element displacement and forces. The strains are assumed to be linearly distributed through the cross-section of the element. Therefore, plane sections are considered to be remain plane during the bending (Taucer et al., 1991). In the model known as Fiber Element Method, the constitutive relation of the cross-sections (integration points) is obtained by using the integration of the behavior of fiber elements. The method that depends on both displacement-based and force-based formulations is used to simulate the nonlinear behavior of RC beam, column, and shear wall elements (Martinelli et al., 2013; Li et al., 2016; Vásquez et al., 2016; Feng and Xu, 2018; Li et al., 2018). However, there are still uncertainties related to the damping ratio and the damping type for the RC structures, the number of integration points used in an element and the fiber element number used in the section.

In this study, nonlinear time-history analyses of the RC shear wall structures are conducted by using the force-based fiber element (FBFE) method. Two different RC structure that consist of shear walls are simulated under the 1994 Northridge and the 1957 San Francisco earthquake loadings. The optimum damping ratio for the stiffness-proportional damping (SPD), mass-proportional damping (MPD), and Rayleigh damping (RD) are investigated. Besides, the optimum fiber element number is determined for the damping types and optimum damping ratio. The numerical analysis results are compared with experimental results in terms of absolute

maximum values of the base overturning moment, the base shear force, and the top displacement. Time-history graphs of top displacement responses for the shear wall structures are also used in the comparisons. The nonlinear seismic analyses are performed by using SeismoStruct (Seismosoft, 2016). The reasonable range of the damping ratio for RC structures with shear walls is determined.

2. Fiber Element Method

The Fiber Element Method represented by both displacement-based and force-based formulations depends on the model of the beam-column element. The uniaxial stress-strain response of the longitudinal fibers that constitute the relation of force-deformation of the section is used in force-based formulations. The method considers the assumption of linear geometry for the plane sections during the deformation. In the method, the nonlinear response of an element is provided by the nonlinearity of fibers stress-strain relation.

In the Fiber Element Method, the structural element is sectioned depending on the integration points (Fig. 1). The number of integration points in an element and the number of fibers (discretization) in a cross-section affect the response of the element, and thereby the response of the structure. Using more fiber elements increases the accuracy of the element behavior as well as increasing the time and effort needed for the computation (Taucer et al., 1991).

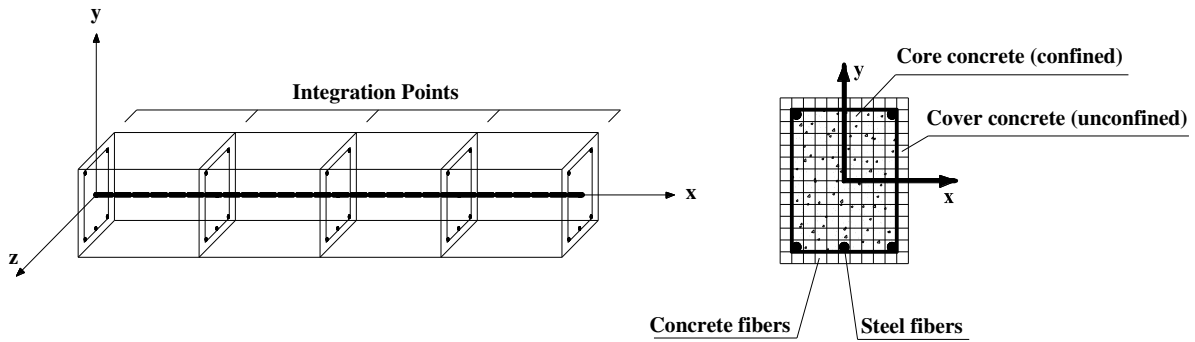


Fig. 1 The fiber beam-column element and discretization of the cross-section (Seismosoft, 2016)

2.1 The Fiber Element Formulation of Beam-Column Element

Force-based fiber element formulation of an element depends on the equilibrium and the force-deformation relation of the sections. Therefore, beam-column fiber elements are developed by using deformation interpolation function, $a(x)$ and force interpolation function, $b(x)$. Element flexibility matrix, \mathbf{F}^{i-1} and a matrix only depending on the interpolation function matrices, \mathbf{T} can be defined in a simpler form as,

$$\mathbf{F}^{i-1} = \left[\int_0^L b^T(x) \cdot \mathbf{f}^{i-1}(x) \cdot b(x) \cdot dx \right] \quad (1)$$

$$\mathbf{T} = \left[\int_0^L b^T(x) \cdot a(x) \cdot dx \right] \quad (2)$$

The element deformation field is represented by the flexibility dependent shape functions by using following equations;

$$a(x) = \mathbf{f}^{i-1}(x) \cdot b(x) \cdot [\mathbf{F}^{i-1}]^{-1} \quad (3)$$

where, \mathbf{f} is flexibility matrix of a section. i denotes iteration number of Newton-Raphson iteration loop at the structural level (Taucer et al. 1991). Thus, \mathbf{f}^{i-1} denotes that flexibility matrix of a section at $(i-1)^{\text{th}}$ Newton-Raphson iteration. Using the interpolation functions, the relation between the section deformations and the element deformations can be drawn as follows;

$$\Delta d^i(x) = \mathbf{f}^{i-1}(x) \cdot b(x) \cdot [\mathbf{F}^{i-1}]^{-1} \Delta q^i \quad (4)$$

where, Δd and Δq are the incremental section deformation and the incremental element deformation, respectively. \mathbf{T} matrix become a 3x3 identify matrix \mathbf{I} by using the special selection of the deformation shape functions. This expression can be proved by the following equation;

$$\mathbf{T} = \left[\int_0^L b^T(x) \cdot a(x) \cdot dx \right] = \left[\int_0^L b^T(x) \cdot \mathbf{f}^{i-1}(x) \cdot b(x) \cdot dx \right] \cdot [\mathbf{F}^{i-1}]^{-1} = \mathbf{I} \quad (5)$$

The deformation interpolation function changes during the iterative solution procedure. Therefore, the method proposed in this study is called as FBE method. The force field is expressed by using section force vector where two bending moments ($M_z(x)$ and $M_y(x)$) are linear and axial force ($N(x)$) is constant (Taucer et al., 1991). Thus, force interpolation function is obtained by result of this expression in a matrix form as;

$$b(x) = \begin{bmatrix} \left(\frac{x}{L}-1\right) & \left(\frac{x}{L}\right) & 0 & 0 & 0 \\ 0 & 0 & \left(\frac{x}{L}-1\right) & \left(\frac{x}{L}\right) & 0 \\ 0 & 0 & 0 & 0 & 1 \end{bmatrix} \quad (6)$$

The force interpolation function, $b(x)$ provides the relation between force distributions along the element with element force vector by using following equation.

$$\Delta \mathbf{D}^i(x) = b(x) \cdot \Delta \mathbf{Q}^i \quad (7)$$

where, $\Delta \mathbf{D}(x)$ and $\Delta \mathbf{Q}$ are incremental section force vector and incremental element force vector, respectively.

The increments of the fiber strain $\Delta \mathbf{e}^j(x)$ are

$$\Delta \mathbf{e}^j(x) = \mathbf{I}(x) \cdot \Delta \mathbf{d}^j(x) \quad (8)$$

where, subscript j is the iteration number at the element level, $\Delta \mathbf{d}^j(x)$ is the given deformation increments and $\mathbf{I}(x)$ is the section compatibility matrix that can be defined as;

$$\mathbf{I}(x) = \begin{bmatrix} -y_1 & z_1 & 1 \\ \mathbf{M} & \mathbf{M} & \mathbf{M} \\ -y_{ifib} & z_{ifib} & 1 \\ \mathbf{M} & \mathbf{M} & \mathbf{M} \\ -y_n & z_n & 1 \end{bmatrix} \quad (9)$$

In this equation, x denotes the location of the integration section along the element longitudinal axis, y_{ifib} and z_{ifib} denote the location of the fiber in the section. Considering the fiber strain increments, the new tangent

modulus E_{ifib}^j and stress σ_{ifib}^j of all fibers are calculated by using the suitable stress-strain relation of fiber. The new tangent stiffness matrix of the section $\mathbf{k}^j(x)$ is determined as follows,

$$\mathbf{k}^j(x) = \mathbf{I}^T(x) \cdot (\mathbf{E}_{tan}^j \mathbf{A}) \cdot \mathbf{I}(x) \quad (10)$$

where, \mathbf{E}_{tan}^j is the tangent modulus that consists of fiber stresses in diagonal matrix form and \mathbf{A} is the diagonal matrix form of the fiber areas A_{ifib} . The new tangent stiffness matrix of the section is can be also stated as,

$$\mathbf{k}^j(x) = \begin{bmatrix} \sum_{ifib=1}^{n(x)} E_{ifib}^j \cdot A_{ifib} \cdot y_{ifib}^2 & \sum_{ifib=1}^{n(x)} E_{ifib}^j \cdot A_{ifib} \cdot y_{ifib} \cdot z_{ifib} & - \sum_{ifib=1}^{n(x)} E_{ifib}^j \cdot A_{ifib} \cdot y_{ifib} \\ \sum_{ifib=1}^{n(x)} E_{ifib}^j \cdot A_{ifib} \cdot y_{ifib} \cdot z_{ifib} & \sum_{ifib=1}^{n(x)} E_{ifib}^j \cdot A_{ifib} \cdot z_{ifib}^2 & \sum_{ifib=1}^{n(x)} E_{ifib}^j \cdot A_{ifib} \cdot z_{ifib} \\ - \sum_{ifib=1}^{n(x)} E_{ifib}^j \cdot A_{ifib} \cdot y_{ifib} & \sum_{ifib=1}^{n(x)} E_{ifib}^j \cdot A_{ifib} \cdot z_{ifib} & \sum_{ifib=1}^{n(x)} E_{ifib}^j \cdot A_{ifib} \end{bmatrix} \quad (11)$$

The new tangent flexibility matrix of the section $\mathbf{f}^j(x)$ is obtained by the inverted form of the new tangent stiffness matrix for the section (Taucer et al., 1991; Martinelli, 2007; Karaton, 2014). In the similar manner, the section resisting forces $\mathbf{D}_R^j(x)$ is determined by the following matrix equation:

$$\mathbf{D}_R^j(x) = \begin{Bmatrix} - \sum_{ifib=1}^{n(x)} \sigma_{ifib}^j \cdot A_{ifib} \cdot y_{ifib} \\ \sum_{ifib=1}^{n(x)} \sigma_{ifib}^j \cdot A_{ifib} \cdot z_{ifib} \\ \sum_{ifib=1}^{n(x)} \sigma_{ifib}^j \cdot A_{ifib} \end{Bmatrix} \quad (12)$$

The numerical results are affected by the material models defined for the nonlinear behavior of the steel and concrete fibers in the sections. In this study, the simulation of the nonlinear response of the reinforcement is achieved by the modified Menegotto and Pinto steel model (Menegotto and Pinto, 1973). Mander-Priestley-Park model (Menegotto and Pinto, 1973) is selected for the material model of the concrete (Fig. 2).

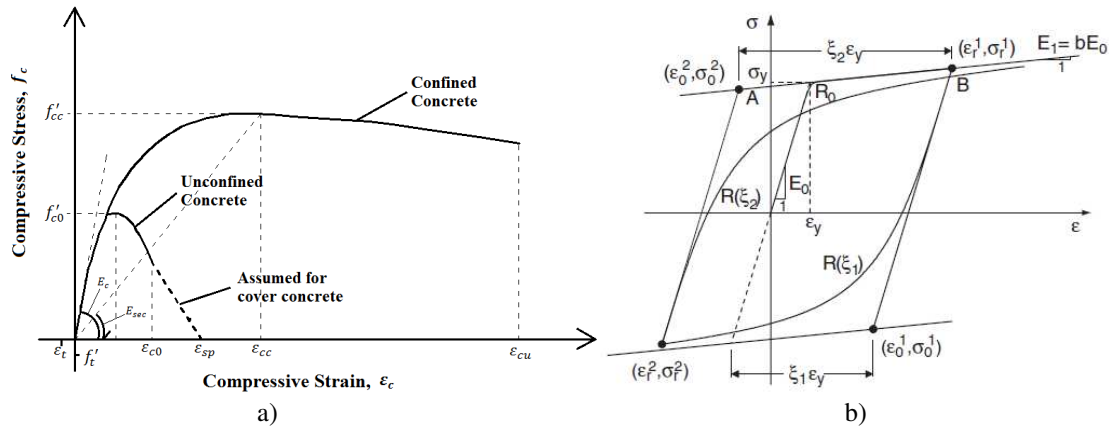


Fig. 2 a) Mander-Priestley-Park concrete model (Mander et al., 1988) and b) Modified Menegotto and Pinto steel model (Kolozvari et al., 2015).

3. Numerical Investigation

The numerical simulations of CAMUS I and NEES-UCSD RC shear wall structures were investigated with the FBE method. The experimental results obtained by previous shaking table tests of these shear wall structures were compared with nonlinear seismic analysis results. For the seismic input, the 1957 San Francisco and the 1994 Northridge earthquake loadings, same as the experimental study are used for the CAMUS I structure and NEES-UCSD structure, respectively (Kazaz et al., 2006; Martinelli, 2007; Martinelli and Filippou, 2009). Seismostruct software was utilized in the nonlinear time-history analyses of the RC shear wall structures by including geometric nonlinearity. In the software, the computation of the nonlinear response of element cross-sections is achieved by the FBE method while the global solutions of the structural element are carried out by the Finite Element Method.

3.1 The structural damping

In this study, the equations of motion for the building are solved by using the Hilber-Hughes-Taylor- α (HHT- α) integration method. Compact form of the equation of motion for the building is given according to HHT- α method as,

$$[M]\{a\}_{i+1} + (1 + \alpha)[C]_{i+1}\{v\}_{i+1} - \alpha[C]_i\{v\}_i + (1 + \alpha)\{F\}_{i+1} - \alpha\{F\}_{i+1} = (1 + \alpha)\{F_g\}_{n+1} - \alpha\{F_g\}_n \quad (13)$$

where $\{u\}$, $\{v\}$, and $\{a\}$ denote the relative displacement, velocity, and acceleration for the structure, respectively. Subscript i shows nonlinear solution step and n shows the external load step; $\{F\}$ indicates the internal load vector; $\{F_g\}$ indicates the external load that formed because of ground acceleration vectors. α is a constant to control the numerical dissipation. $[C]$ and $[M]$ show damping matrix and mass matrix of the structure. Damping matrix represents structural damping in numerical analysis. The matrix is obtained by stiffness matrix ($[K]$) and the mass matrix as,

$$[C]_i = \alpha_c \cdot [M] + \beta_c \cdot [K]_i \quad (14)$$

where, β_c and α_c are coefficients for the stiffness matrix and the mass matrix, respectively (Calayir and Karaton, 2005).

The damping ratio varies between 1% and 10% in a typical RC structure except for the special cases (Celep and Kumbasar, 2004). The damping ratio is generally assumed as 5% in numerical analyses of the structures. In most of the building codes, seismic design spectra are defined with respect to 5% damping ratio. However, based on the findings of Fritz et al. (2009), it was also recommended that the damping ratio can be selected as 3% in the numerical analysis of the RC shear walls subjected to earthquake loading in all vibration modes (Gilles and McClure, 2012). The dynamic properties of 27 different RC shear wall structures were obtained in accordance with the ambient vibration test results. The mean of the damping ratios that vary between 1% and 4% was computed as 2%. It was also concluded that the critical range of the damping ratio was 3%-4% (Gilles and McClure, 2012).

In this study, properly using the damping ratio and the damping type in the numerical analyses of the RC shear wall structures are investigated for the FBE method. The SPD, MPD, and RD types for structural damping are selected and the damping ratio is changed between 2% and 5%.

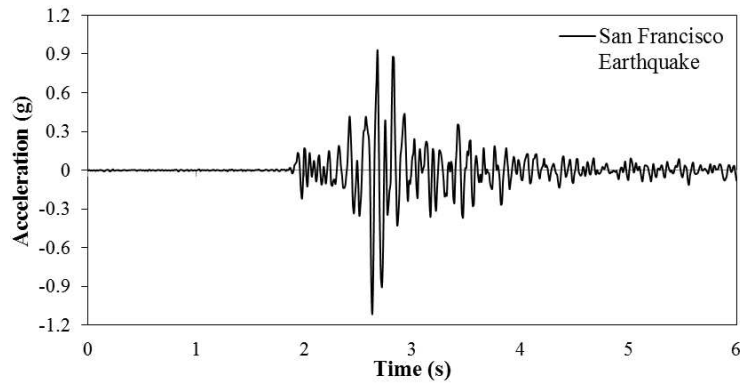


Fig. 4 The scaled 1957 San Francisco earthquake loading (Kazaz et al., 2006)

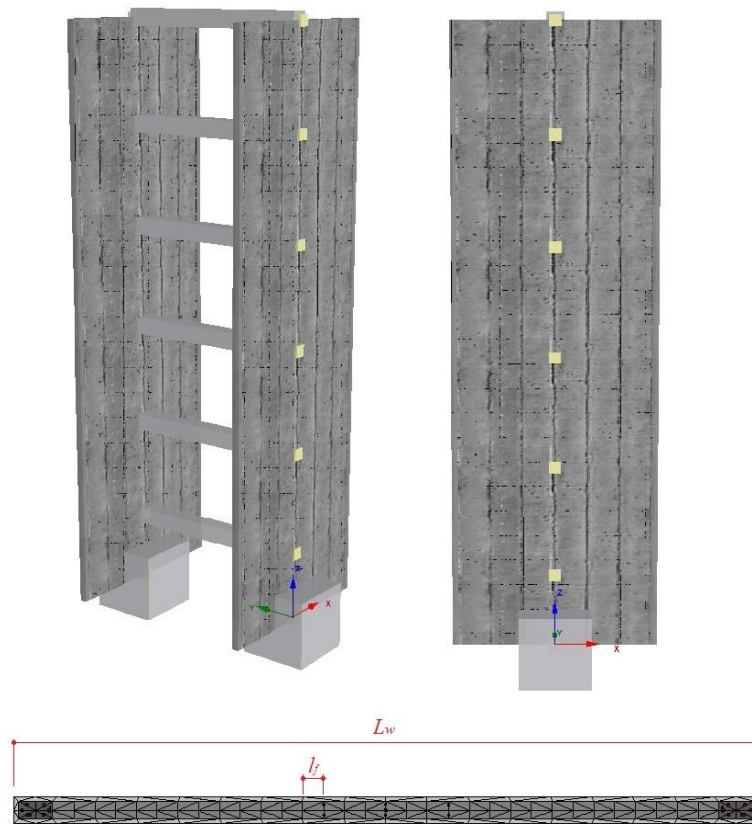


Fig. 5 3D view of the CAMUS I structure model and meshing of the shear wall

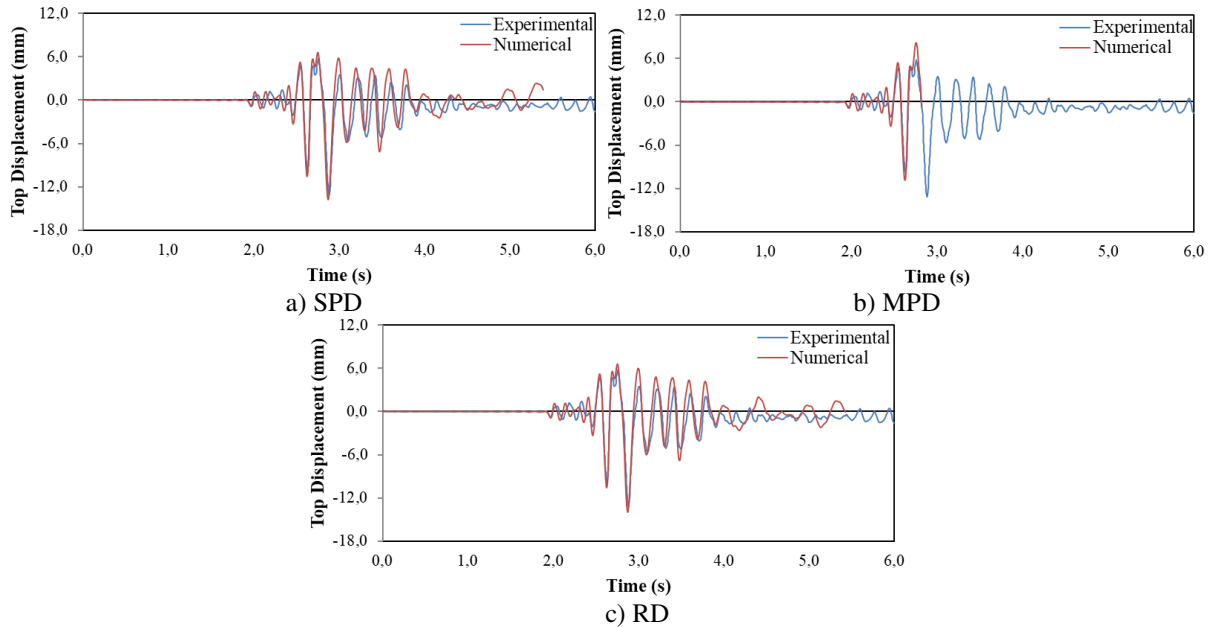
Results of experimental and numerical analysis were compared according to maximum absolute overturning moment, base shear force, and top displacement values. The time-history graphs of the top displacement responses are also examined for comparisons. The fiber element number, the damping type, and damping ratio were considered as variable parameters. The number of fiber elements was 250 for the first solution phase. This value was changed in order to observe the efficiency of the FBFEM method on the seismic behavior of RC shear wall structures. The sectional properties of the shear wall and meshing of the fiber elements are illustrated in Fig. 5. The mean length of fiber elements and the longitudinal length of the shear wall are symbolized by l_f and L_w (Fig. 5), respectively.

Table 1 Eigenvalue analysis results of the CAMUS I

Mode	Period	U_x (%)	U_y (%)	U_z (%)	R_x (%)	R_y (%)	R_z (%)
1	0.824014	0.00	64.01	0.00	34.21	0.00	0.00
2	0.136323	0.00	19.72	0.00	14.93	0.00	0.00
3	0.121107	70.45	0.00	0.00	0.00	1088.45	0.00
4	0.119675	0.00	0.00	0.00	0.00	0.00	1028.37
5	0.090578	0.00	0.10	0.00	0.18	0.00	0.00
6	0.049915	0.00	6.49	0.00	8.16	0.00	0.00
7	0.026083	0.00	3.34	0.00	5.12	0.00	0.00
8	0.022528	0.00	3.11	1.63	5.06	0.00	0.00
9	0.019420	19.88	0.00	0.00	0.00	254.70	0.00
10	0.019389	0.00	0.00	0.00	0.00	0.00	288.92
11	0.006804	5.08	0.00	0.00	0.00	114.07	0.00
12	0.005995	0.00	0.05	84.08	0.09	0.00	0.00
13	0.003387	1.58	0.00	0.00	0.00	43.54	0.00
14	0.003310	0.00	5.01	0.05	8.90	0.00	0.40
15	0.002081	0.42	0.00	0.00	0.00	12.92	0.00
16	0.000969	2.59	0.00	0.00	0.00	89.81	0.00

The bold values show the maximum mass participation ratio and the related periods.

Eigenvalue analysis was achieved in order to determine the natural frequency of the shear wall. Effective modal mass percentages are shown in Table 1. In this table, U_x , U_y and U_z represent the displacements in the x , y and z directions, respectively. R_x , R_y and R_z are the rotations around x , y and z axes, respectively. As seen in Table 1, mode 3 has the highest mass participation ratio. Natural frequency of mode 3 was selected for the SPD and MPD computations. However, the natural frequency of mode 1 that has the second highest value, was also used for the RD computation.

**Fig. 6** Top displacement responses of the CAMUS I for the damping ratio of 2%

Roof displacement time-history graphs obtained from numerical analysis results of the CAMUS I structure were acquired at the 2%, 3%, and 5% damping ratios using the San Francisco earthquake loading. Comparisons of experimental and numerical results were given in Figs. 6-8. Numerical solutions for SPD, MPD and RD with 2% damping ratio was converged until $t=5.38$ sec., $t=2.81$ sec. and $t=5.41$ sec., respectively. Although solution for MPD cannot be obtained after $t=4.33$ sec., solutions for SPD and RD were completed for

3% damping ratio. Solutions for SPD and MPD at 5% damping ratio was not converged at $t=4.84$ sec., $t=2.72$ sec., respectively. In this damping ratio, only numerical solution with RD was completed for all earthquake-loading steps.

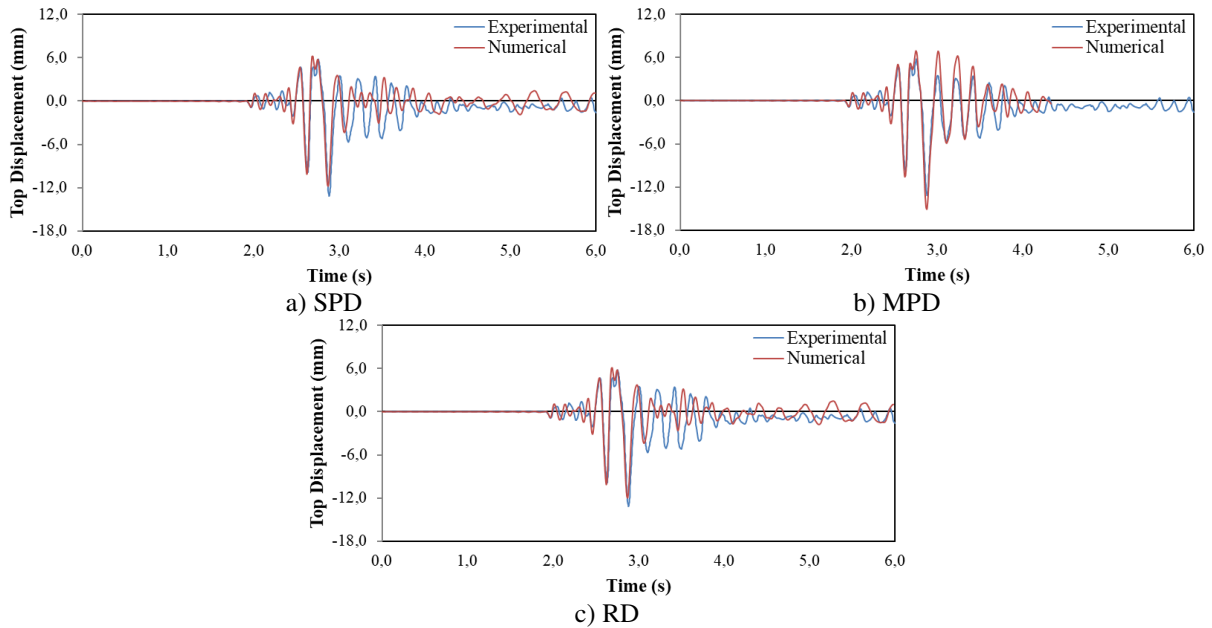


Fig. 7 Top displacement responses of the CAMUS I for the damping ratio of 3%

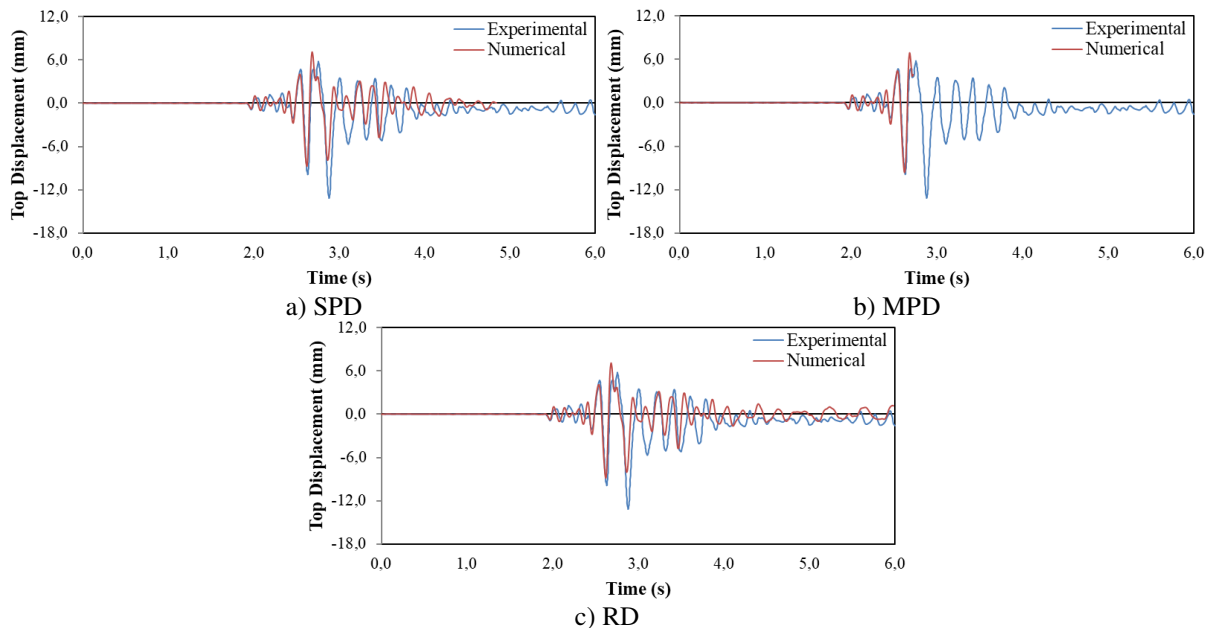


Fig. 8 Top displacement responses of the CAMUS I for the damping ratio of 5%

Experimental and numerical results are compared in Table 2 for damping ratios changing between 2-5%, and for three damping types. In this table, the least differences of the absolute maximum top displacement values between numerical and experimental analysis for SPD, MPD, and RD types were defined as 0.21% at 2.5% damping ratio, 0.85% at 4.5% damping ratio, and 3.16% at 2.5% damping ratio, respectively. The minimum differences of the absolute maximum base shear force values between numerical and experimental

analysis for SPD, MPD, and RD types were obtained as 0.27% at 2% damping ratio, 2.86% at 5.0% damping ratio, and 0.84% at 4.5% damping ratio, respectively. Additionally, the minimum differences of the absolute maximum base overturning moment values between numerical and experimental analysis results for SPD, MPD, and RD types were obtained as 7.28%, 1.93% and 7.68% at 2.5% damping ratio, respectively.

Table 2 The absolute maximum values obtained by numerical analyses and the comparison with experimental results of the CAMUS I structure for the damping ratios that vary between 2% and 5%

Damping		Top Displacement		Base Shear Force		Overturning Moment	
Damping Type	Damping Ratio (%)	Absolute maximum (mm)	Difference between Exp. and Num. Analysis (%)	Absolute maximum (kN)	Difference between Exp. and Num. Analysis (%)	Absolute maximum (kN.m)	Difference between Exp. and Num. Analysis (%)
SPD	2.0	13.78	4.42	111.69	0.27	299.61	7.53
	2.5	13.17	0.21	107.60	3.93	300.41	7.28
	3.0	11.76	10.89	107.25	4.24	297.67	8.13
	3.5	10.42	21.05	106.93	4.53	296.66	8.44
	4.0	9.40	28.75	106.59	4.83	296.42	8.51
	4.5	9.08	31.22	111.33	0.60	295.90	8.67
	5.0	8.79	33.36	115.14	2.80	299.82	7.46
MPD	2.0	10.84	17.82	151.44	35.22	291.86	9.92
	2.5	16.35	23.93	132.89	18.65	330.25	1.93
	3.0	15.12	14.62	156.85	40.04	331.14	2.20
	3.5	10.46	20.72	131.80	17.68	289.52	10.64
	4.0	13.80	4.56	201.07	79.53	298.53	7.86
	4.5	13.08	0.85	127.64	13.97	297.01	8.33
	5.0	9.59	27.32	108.80	2.86	293.27	9.49
RD	2.0	14.03	6.32	115.32	2.96	298.37	7.91
	2.5	12.78	3.16	106.29	5.10	299.12	7.68
	3.0	12.04	8.78	107.24	4.25	296.71	8.42
	3.5	10.76	18.44	106.04	5.32	292.33	9.77
	4.0	9.73	26.24	106.41	4.99	294.11	9.23
	4.5	9.16	30.58	111.06	0.84	291.08	10.16
	5.0	8.84	33.03	116.92	4.39	295.16	8.90

The bold values show the minimum differences.

The damping ratio and the damping type were changed for the calibration of the model. Several values between 2% and 5% damping ratios were considered for three damping types. Numerical results show that the difference was 0.05% at 2.49% damping ratio for the type of SPD. This numerical result was converged until 5.73 sec. A difference of 0.03% was calculated for the type of MPD at 4.52% damping ratio (Fig. 9).

In the calculation of RD coefficients, combinations of 2.49% and 4.52% damping ratios, and natural frequencies of modes 1 and 3 were considered. Mode 3 for the first natural frequency at 2.49% damping ratio, mode 1 for the second natural frequency at 4.52% damping ratio were used in the first combination. Difference between numerical and experimental analysis results was observed as 2.11% for this combination. In the second combination, mode 3 for the first natural frequency at 4.52% damping ratio, mode 1 for the second natural frequency at 2.49% damping ratio were used. Difference between numerical and experimental results was calculated as 30.99% for the second combination. Numerical solutions for the first and the second combinations

converged until 4.81 and 4.52 sec., respectively (Fig. 10). The first approximation has given better results than the second.

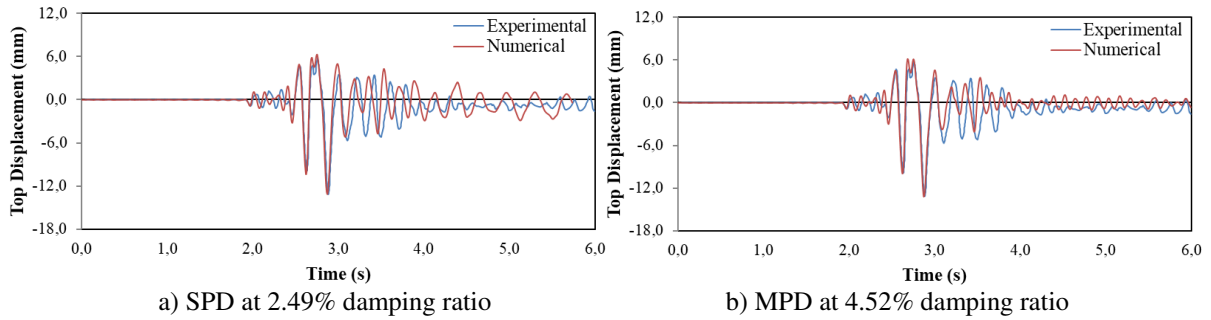


Fig. 9 Top displacement responses of the CAMUS I for SPD and MPD types at the optimum damping ratios

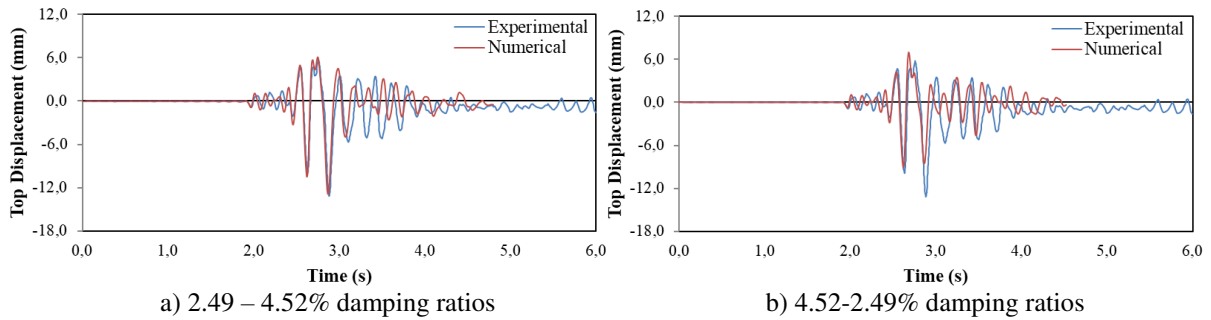


Fig. 10 Top displacement responses of the CAMUS I for RD at the optimum damping ratios of the first two effective modes

Comparisons between damping types were implemented with respect to differences between numerical and experimental results regarding base shear force, absolute maximum roof displacement and overturning moment. For the roof displacement, provided that the damping ratio is between 2.5% and 3%, the differences are less than 10.9% (except for MPD). The differences are less than 5.1% (except for MPD) for the base shear forces and less than 8.5% for the overturning moments (Fig.11).

Nonlinear seismic analysis results exhibited good fit with the experimental results between 2.5 and 3.1 seconds. Amplitude and frequency divergences were seen after 3.1 seconds. Therefore, the time interval of 2.5 and 3.1 seconds was considered for the comparison of the top displacement time history graphs. Differences of roof displacement between numerical and experimental analysis are determined less than 3% at 2.49%, 4.52% and 2.49-4.52% damping ratios for SPD, MPD and RD types, respectively. These three cases, which exhibit the best approximation within all analysis, were used during the investigation of the optimum l_f/L_w ratio (optimum fiber element number). Fiber element number was modified to 100, 500, 750 and 1000 instead of 250. Numerical results with respect to the l_f/L_w ratios are given in Table 3.

The optimum ratios of l_f/L_w were determined as 2.78% (250 fiber elements) for SPD and MPD types, as 11.20% (100 fiber elements) for RD type. Minimum differences between the absolute maximum roof displacement values of the CAMUS I structure obtained from the numerical and experimental analysis for SPD, MPD and RD solutions were computed as 0.05% at 2.49% damping ratio, 0.03% at 4.52% damping ratio and 0.41% at 2.49-4.52% damping ratios, respectively. On the other hand, when the l_f/L_w ratio is selected less than 2.78% for the CAMUS I shear wall, differences of the roof displacement are less than 1% for SPD type in the FBFE method.

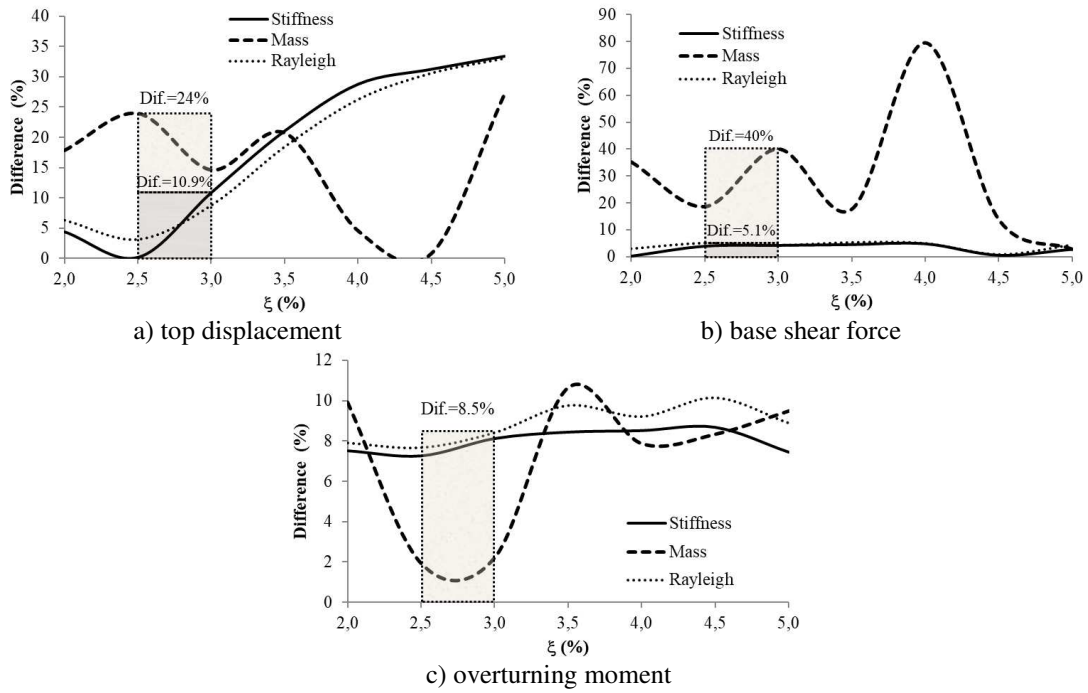


Fig. 11 Comparisons of absolute maximum values obtained by numerical analysis with experimental results of the CAMUS I structure for various damping types

Table 3 Comparison of absolute maximum top displacement values of CAMUS I structure for various number of fiber elements

Fiber Element Number	l_f/L_w Ratio (%)	Absolute Maximum Top Displacement (mm)			Difference between Numerical Analysis and Experimental Results (%)		
		SPD 2.49%	MPD 4.52%	RD 2.49-4.52%	SPD 2.49%	MPD 4.52%	RD 2.49-4.52%
100	11.20	12.83	13.51	13.25	2.785	2.350	0.405
250	2.78	13.19	13.20	12.92	0.053	0.030	2.114
500	1.14	13.17	12.56	12.87	0.154	4.792	2.465
750	0.76	13.10	13.09	12.87	0.683	0.774	2.460
1000	0.62	13.12	12.99	12.87	0.601	1.560	2.483

The bold values show the minimum differences.

3.3 Numerical Analysis of the NEES-UCSD Shear Wall

A reinforced concrete shear wall structure constructed as seven-story by NEES (Network for Earthquake Engineering Simulation). It was seismically loaded on a shaking table at University of California at San Diego (UCSD) (Martinelli, 2007). This structure is composed of two types of shear walls located on the central axis and pier columns located on the corners of the structure. One of the shear walls is called as the web wall, while the other one is called as the flange wall. The walls were built as perpendicular to each other. The slab is connected to the flange wall and two shear walls are joined by slotted connections. The heights of basement and each floor are 0.76 m and 2.74 m, respectively. Total height of the structure is 19.96 m. The structure is fastened to the ground and its mass is 226 tons. Cross-sections of the flange wall and the web wall are different from each other. The width of the flange wall is 4.88 m and the thicknesses of the flange wall are 203 mm and 152 mm for the last floor and other floors, respectively. The width of the web wall is 3.65 m and the thickness of the web

was 6.7 according to the measured energy release. It can be observed from Fig. 13 that high acceleration values located on limited time intervals of the earthquake and its PGA value is 0.83g (Martinelli, 2007). According to experimental study, absolute maximum values of overturning moment and the shear force were determined at the base level as 11839.4 kN·m and 1184.7 kN, respectively. The absolute maximum values of displacement were measured as 395 mm at the top of the structure.

In the seismic analysis of the NEES-UCSD structure using the FBE method, 14 elements and 56 nodes were used for the model. The finite element model of the structure is illustrated in Fig. 14. Each element had four integration points. The maximum iteration numbers for the element solution and the global solution were 300 and 50, respectively.

Experimental results were compared with the numerical analysis results regarding the absolute maximum base overturning moment, base shear force, and roof displacement values, and time-history graphs of roof displacement of the structure. 250 fiber element numbers were chosen in the first solution stage. Thereafter, the number of fiber elements was modified in order to determine the ratio of optimum fiber element length.

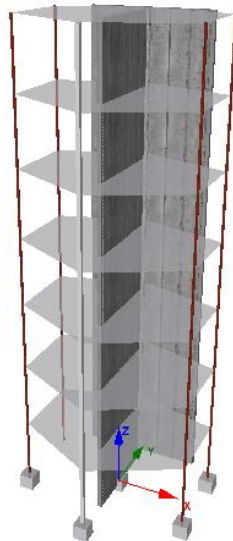


Fig. 14 3D view of the NEES-UCSD structure model

The natural frequencies for the structure were calculated according to percentages of effective modal mass and modal analysis results are shown in Table 4. As seen the table, the mass participation ratio of mode 3 was calculated as the highest value within all modes. Therefore, mode 3 was taken into consideration in the SPD and MPD calculations. In the RD computation, the natural frequencies of mode 3 and 4 were considered, since mass participation ratio of mode 4 has the second highest value within other modes.

Tangent stiffness matrix of the structure was used in order to calculate its damping matrix. Comparisons of numerical analysis and experimental results were conducted in terms of top displacement time-history graphs. The graphs were given in Figs. 15-17 for three damping ratios with SPD, MPD and RD types. The numerical convergence is observed for all steps of the nonlinear time-history analyses of the NEES-UCSD shear wall structure.

Table 4 Eigenvalue analysis results of the NEES-UCSD

Mode	Period	U _x (%)	U _y (%)	U _z (%)	R _x (%)	R _y (%)	R _z (%)
1	1.005847	0.00	0.01	0.06	0.13	0.00	0.06
2	0.514932	23.68	0.00	0.00	0.00	9.85	42.09
3	0.473033	0.00	64.37	0.00	30.76	0.00	0.00
4	0.248135	41.24	0.00	0.00	0.00	18.14	23.11
5	0.237939	0.00	0.14	0.01	0.24	0.04	0.68
6	0.085337	6.96	0.00	0.00	0.00	8.55	13.18
7	0.084365	0.00	0.00	48.48	0.01	0.00	0.00
8	0.077571	0.00	20.62	0.00	24.22	0.00	0.00
9	0.040835	13.60	0.00	0.00	0.00	14.75	6.96
10	0.030640	2.22	0.00	0.00	0.00	4.23	4.74
11	0.028455	0.00	0.00	5.08	0.00	0.00	0.00
12	0.028036	0.00	7.24	0.00	13.77	0.00	0.00
13	0.023701	0.00	0.87	0.02	6.07	0.00	0.00
14	0.022999	0.00	0.94	6.21	0.30	0.00	0.00
15	0.022942	0.00	0.37	10.29	5.10	0.00	0.00
16	0.020645	0.00	0.00	24.26	1.83	0.00	0.00
17	0.017759	0.00	0.01	1.64	0.12	0.00	0.00
18	0.015711	1.72	0.00	0.00	0.00	3.65	1.84
19	0.014860	0.00	0.09	0.62	0.85	0.00	0.00
20	0.014813	4.27	0.00	0.00	0.00	7.39	2.99
21	0.011901	0.00	0.04	0.72	0.23	0.00	0.00
22	0.009637	0.78	0.00	0.00	0.01	1.84	1.22
23	0.007607	2.54	0.03	0.01	0.05	5.43	0.93
24	0.007199	0.01	0.01	5.17	0.01	0.03	0.00
25	0.005184	1.40	0.30	0.01	0.64	3.40	0.06
26	0.001695	0.46	0.83	0.01	1.77	1.04	2.34

The bold values show the maximum mass participation ratio and the related periods.

The differences between numerical analysis obtained for the SPD, MPD, and RD types and experimental results are given in Table 5 for the damping ratios that vary between 2% and 5%. The least differences of the absolute maximum roof displacement values between numerical and experimental results for SPD, MPD, and RD types were obtained as 1.56% at 3.5% damping ratio, 0.58% at 3.0% damping ratio and 0.25% at 3.0% damping ratio, respectively. The minimum differences of the absolute maximum base shear force values between numerical and experimental results for SPD, MPD, and RD types were obtained as 13.46% at 5.0% damping ratio, 23.08% at 5.0% damping ratio and 21.33% at 4.5% damping ratio, respectively. Additionally, the minimum differences of the absolute maximum base overturning moment values between numerical and experimental results for SPD, MPD, and RD types were obtained as 26.92% at 5.0% damping ratio, 34.84% at 2.0% damping ratio and 34.58% at 2.0% damping ratio, respectively.

The damping ratio and the damping type were changed to obtain the best approximation to experimental results. The differences were 0.29% and 0.58% between numerical and experimental results for SPD with damping ratio of 3.25% and for MPD with damping ratio of 3%, respectively (Fig. 18). The RD coefficients were calculated by combinations of 3.25% and 3.00% damping ratios for natural frequencies of modes 3 and 4. Solutions were obtained for 3.25% and 3.00% damping ratios with the natural frequencies of modes 3 and 4, in the first combination, respectively. In the second combination, damping ratios of 3% and 3.25% were used for the natural frequencies of modes 3 and 4, respectively. Time-history graphs for the first and the second combinations are shown in Fig. 19. Differences of 2.48% and 0.08% were observed between numerical analysis and experimental results in the first and the second combinations, respectively.

Table 5 The absolute maximum values obtained by numerical analyses and the comparison with experimental results of the CAMUS I structure for the damping ratios that vary between 2% and 5%

Damping		Top Displacement		Base Shear Force		Overturning Moment	
Damping Type	Damping Ratio (%)	Absolute maximum (mm)	Difference between Exp. and Num. Analysis (%)	Absolute maximum (kN)	Difference between Exp. and Num. Analysis (%)	Absolute maximum (kN.m)	Difference between Exp. and Num. Analysis (%)
SPD	2.0	434.85	10.09	942.75	20.42	8171.53	30.98
	2.5	418.04	5.83	979.25	17.34	8205.66	30.69
	3.0	401.69	1.69	999.35	15.65	8310.17	29.81
	3.5	388.83	1.56	980.59	17.23	8474.23	28.42
	4.0	374.83	5.11	992.87	16.19	8389.46	29.14
	4.5	359.01	9.11	979.15	17.35	8401.22	29.04
	5.0	345.90	12.43	1025.18	13.46	8652.01	26.92
MPD	2.0	427.26	8.17	751.57	36.56	7714.63	34.84
	2.5	408.92	3.52	768.55	35.13	7617.18	35.66
	3.0	392.71	0.58	777.33	34.39	7513.34	36.54
	3.5	375.82	4.86	789.08	33.39	7420.86	37.32
	4.0	355.81	9.92	887.28	25.11	7372.18	37.73
	4.5	344.82	12.70	871.59	26.43	7391.74	37.57
	5.0	331.37	16.11	911.29	23.08	7356.02	37.87
RD	2.0	428.05	8.37	817.91	30.96	7745.92	34.58
	2.5	410.01	3.80	854.18	27.90	7678.84	35.14
	3.0	394.00	0.25	862.50	27.20	7629.64	35.56
	3.5	378.89	4.08	901.33	23.92	7591.59	35.88
	4.0	363.86	7.88	924.58	21.96	7505.11	36.61
	4.5	351.16	11.10	931.99	21.33	7460.55	36.99
	5.0	338.93	14.19	930.80	21.43	7445.20	37.12

The bold values show the minimum differences.

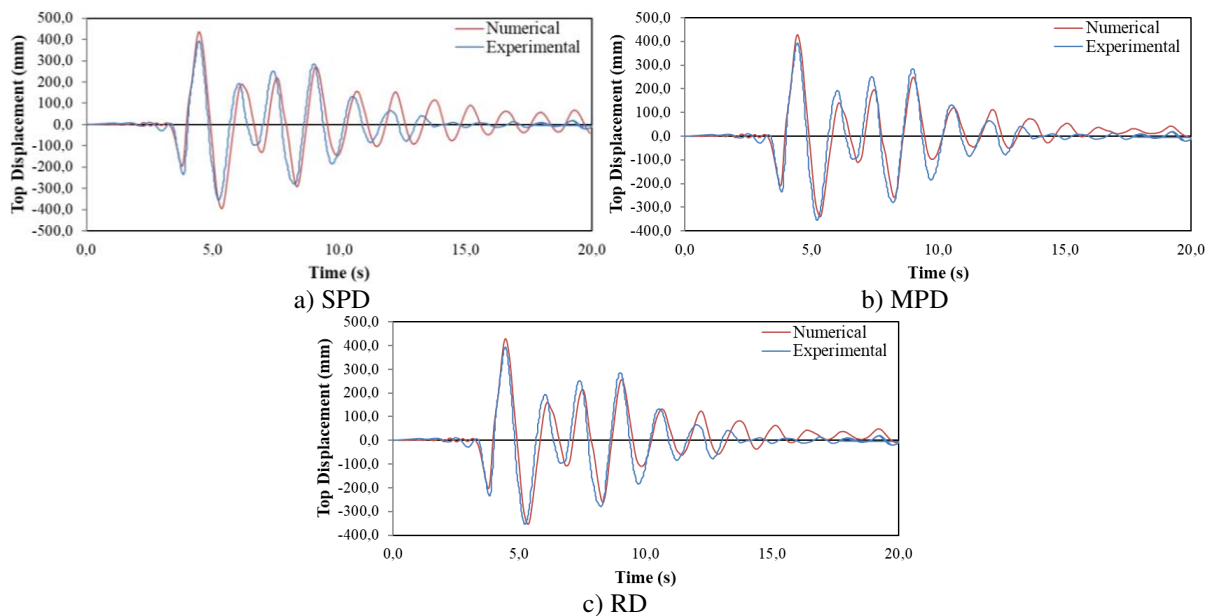


Fig. 15 Top displacement responses of the CAMUS I for the damping ratio of 2%

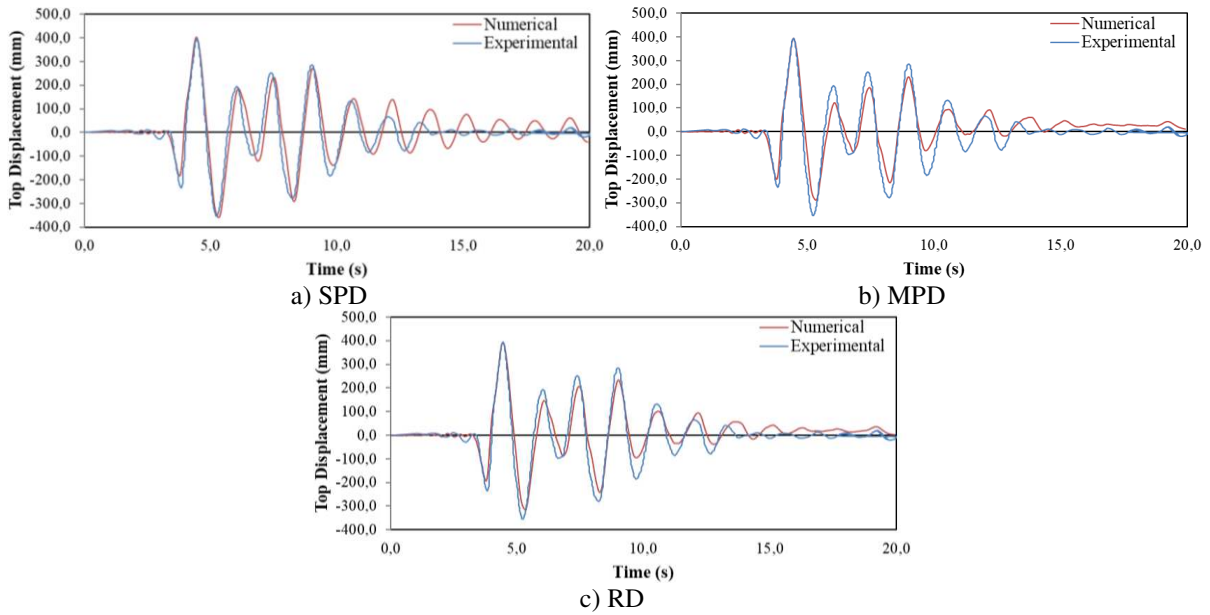


Fig. 16 Top displacement responses of the CAMUS I for the damping ratio of 3%

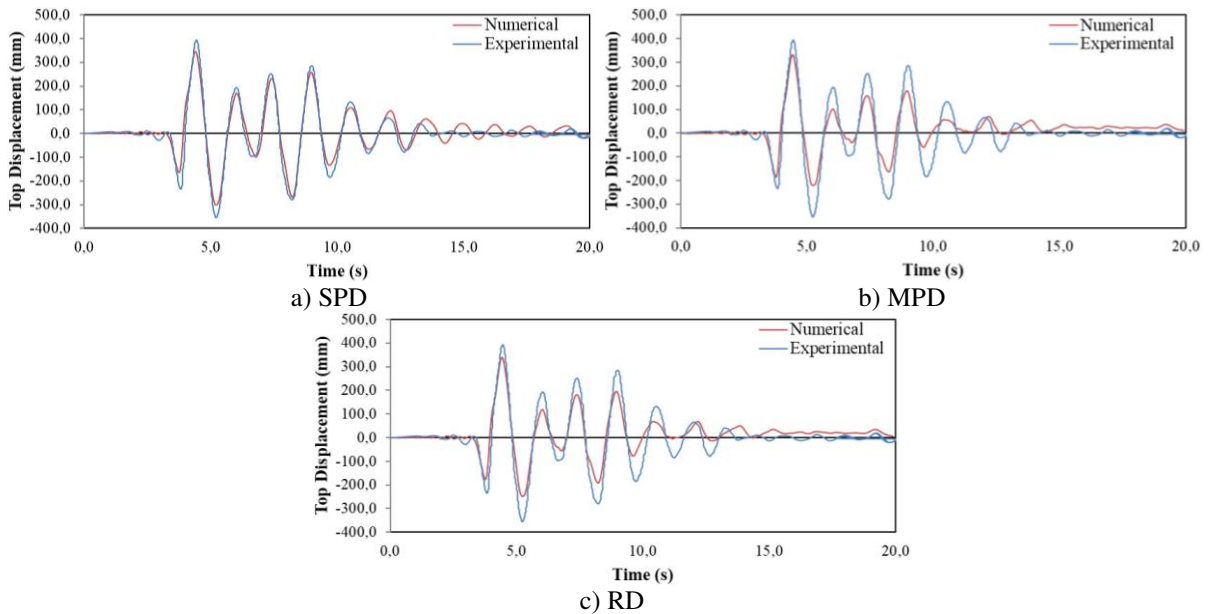


Fig. 17 Top displacement responses of the CAMUS I for the damping ratio of 5%

The damping types were compared with respect to differences between numerical and experimental results considering absolute maximum base overturning moment, base shear force, and roof displacement. For the roof displacements, provided that the damping ratio is between 2.5% and 3.5%, the differences are defined less than 5.9%. The differences for the base shear forces and the overturning moments were defined less than 35.2% and 37.4%, respectively (Fig. 20).

Nonlinear seismic analysis results exhibited good fit with the experimental results between 4 and 10 seconds. Amplitude and frequency discrepancies were seen after 10 seconds. Therefore, the time interval of 4 and 10 seconds was considered for the comparison of the top displacement graph. Non-significance differences were observed between solutions for the last four conditions; SPD at 3.25% damping ratio, MPD at 3.00% damping ratio, RD at 3.00-3.25% damping ratios and RD at 3.25-3.00% damping ratios. Differences of top displacement values are less than 1% in first three conditions. Optimum fiber element number was specified by

taking into account results of these three conditions. 70, 80, 90, 100, 250, 500, 750 and 1000 fiber elements were used and obtained numerical results were given with the l_f/L_w ratio in Table 6.

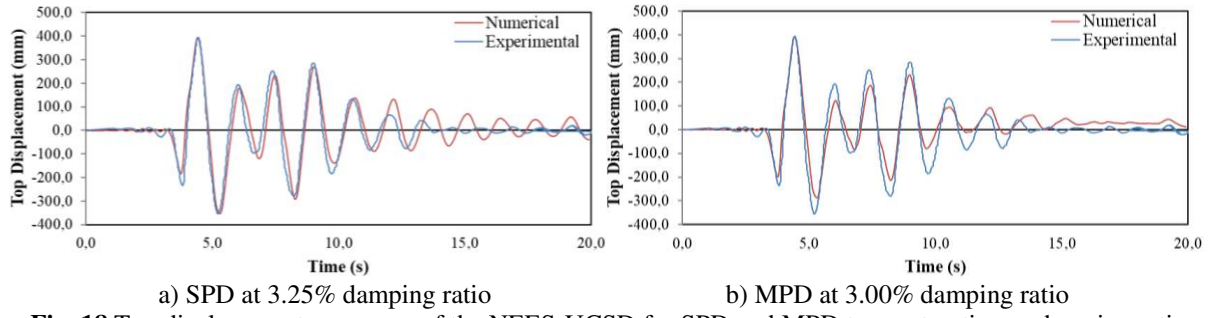


Fig. 18 Top displacement responses of the NEES-UCSD for SPD and MPD types at optimum damping ratios

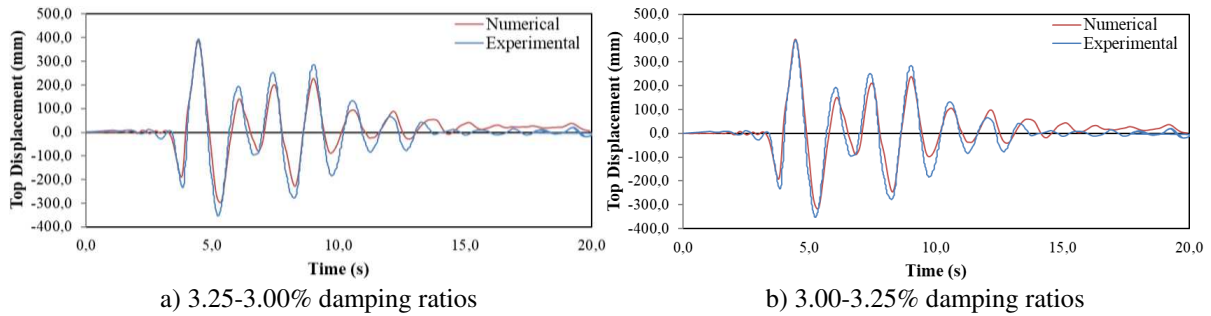


Fig. 19 Top displacement responses of the NEES-UCSD for RD type at the optimum damping ratios of the first two effective modes

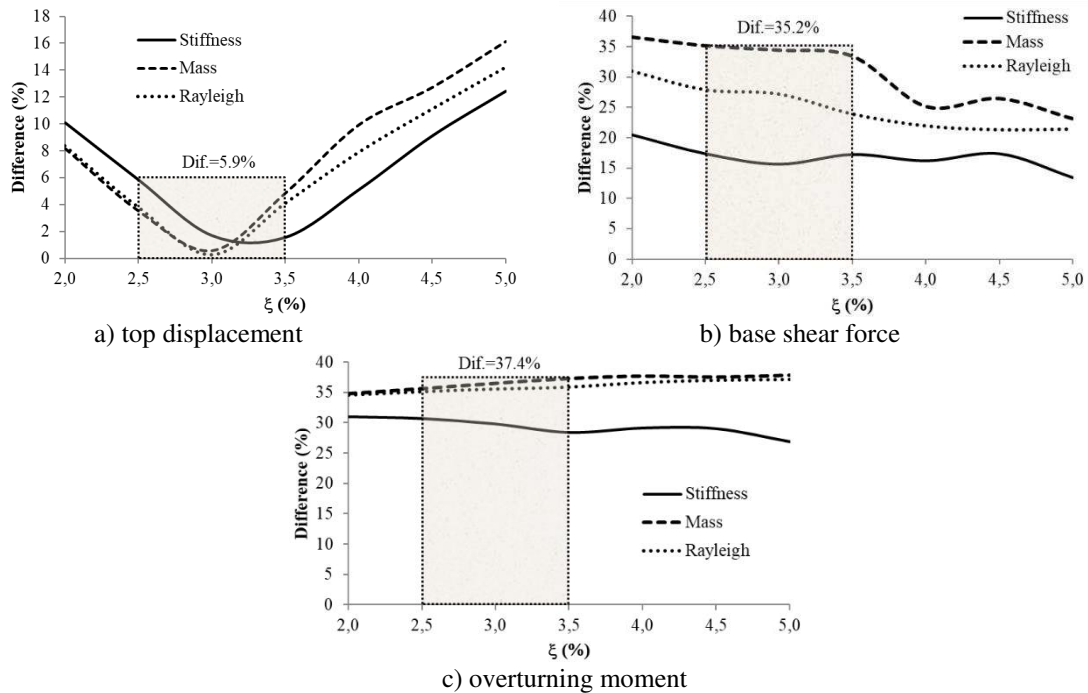


Fig. 20 Comparisons of absolute maximum values obtained by numerical analysis with experimental results of the NEES-UCSD structure for various damping types

The optimum ratios of l_f/L_w for SPD, MPD, and RD types were determined as 15.20% (90 fiber elements), 10.87% (100 fiber elements), and 2.81% (250 fiber elements), respectively. The least differences of the roof displacement values between numerical and experimental results by using these optimum l_f/L_w ratios

are calculated as 0.034%, 0.041%, and 0.079% for SPD, MPD, and RD types, respectively. Differences regarding the roof displacement are less than 0.7% for all the damping types in the FBFE method, provided that fiber element length is selected less than 10.87% of longitudinal length of shear wall (100 or more number of fiber element).

Table 6 Comparison of absolute maximum top displacement values of NEES-UCSD structure for various number of fiber elements

Fiber Element Number	l_f/L_w Ratio (%)	Absolute Maximum Top Displacement (mm)			Difference between Numerical Analysis and Experimental Results (%)		
		SPD 3.25%	MPD 3.00%	RD 3.0-3.25%	SPD 3.25%	MPD 3.00%	RD 3.0-3.25%
70	43.50	400.85	391.18	401.28	1.481	0.968	1.591
80	21.75	396.47	390.17	396.87	0.373	1.224	0.474
90	15.20	395.13	390.36	397.63	0.034	1.175	0.666
100	10.87	393.87	395.16	396.07	0.286	0.041	0.270
250	2.81	393.87	392.71	394.69	0.286	0.581	0.079
500	1.36	393.80	392.49	394.22	0.303	0.636	0.198
750	0.98	396.10	392.41	394.05	0.280	0.656	0.241
1000	0.71	395.82	392.78	394.13	0.209	0.563	0.221

The bold values show the minimum differences.

3.4 Comparison of CAMUS I and NEES-UCSD shear wall structures

Comparison of NEES-UCSD and CAMUS I shear wall structures were achieved to investigate the efficiency of FBFE method. In the comparisons, the absolute maximum values of the overturning moment, the base shear force and the roof displacement were used for all damping types and the damping ratios that selected between 2% and 5%.

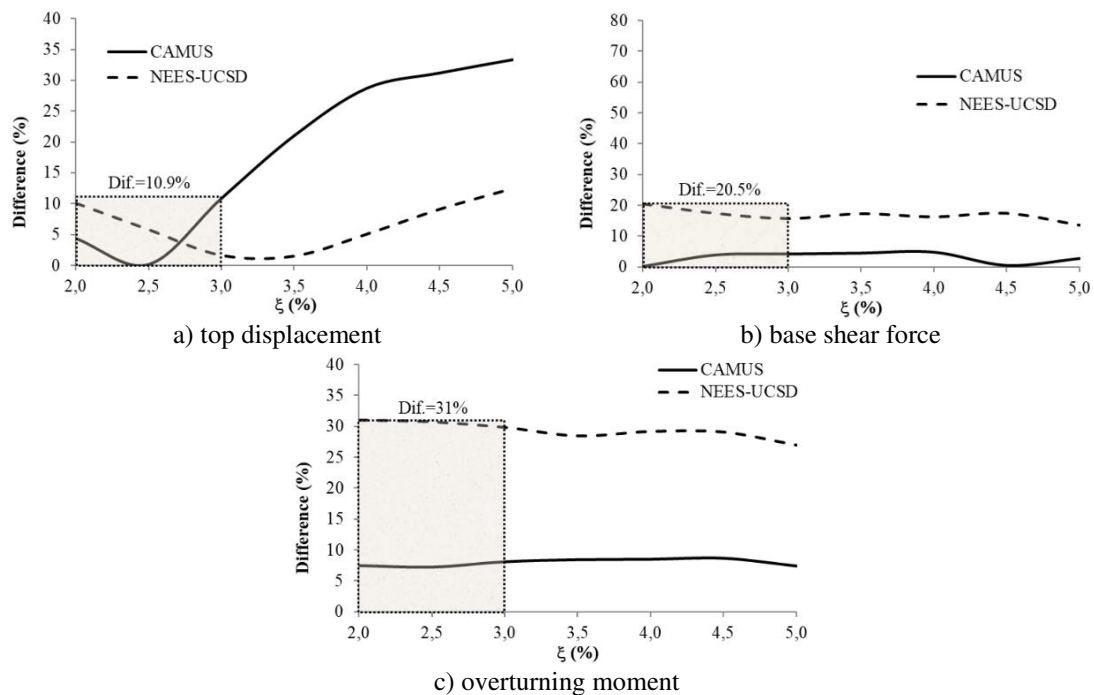


Fig. 21 Comparisons of absolute maximum values obtained by numerical analysis with experimental results of the both shear wall structures for SPD

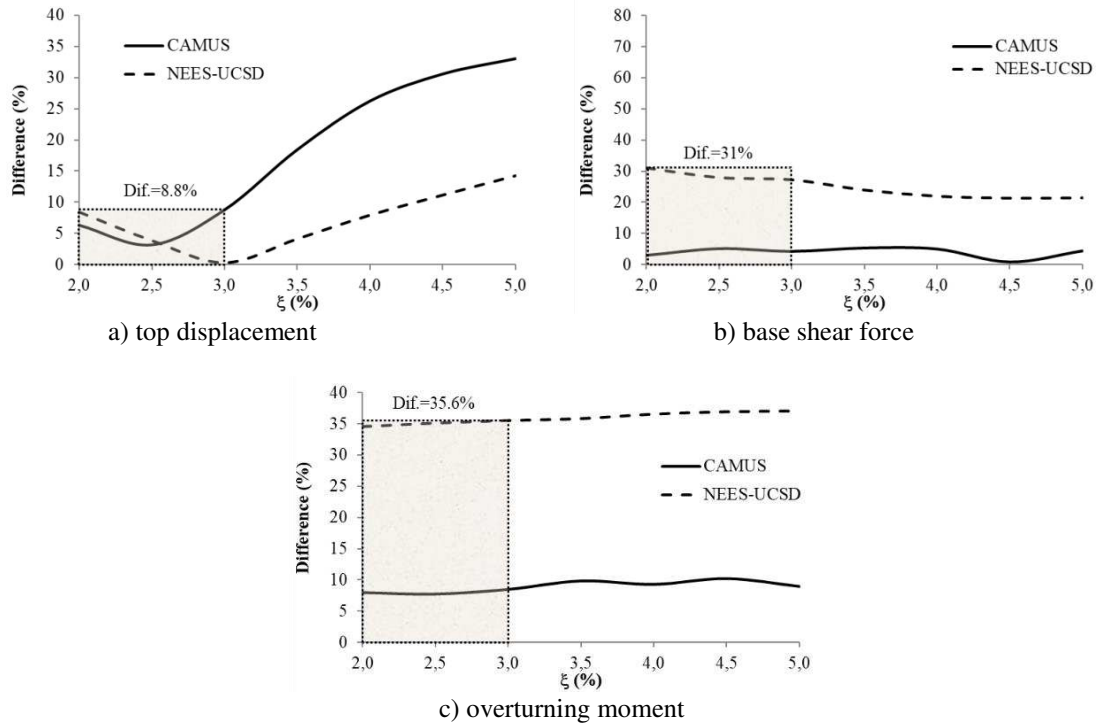


Fig. 22 Comparisons of absolute maximum values obtained by numerical analysis with experimental results of the both shear wall structures for RD

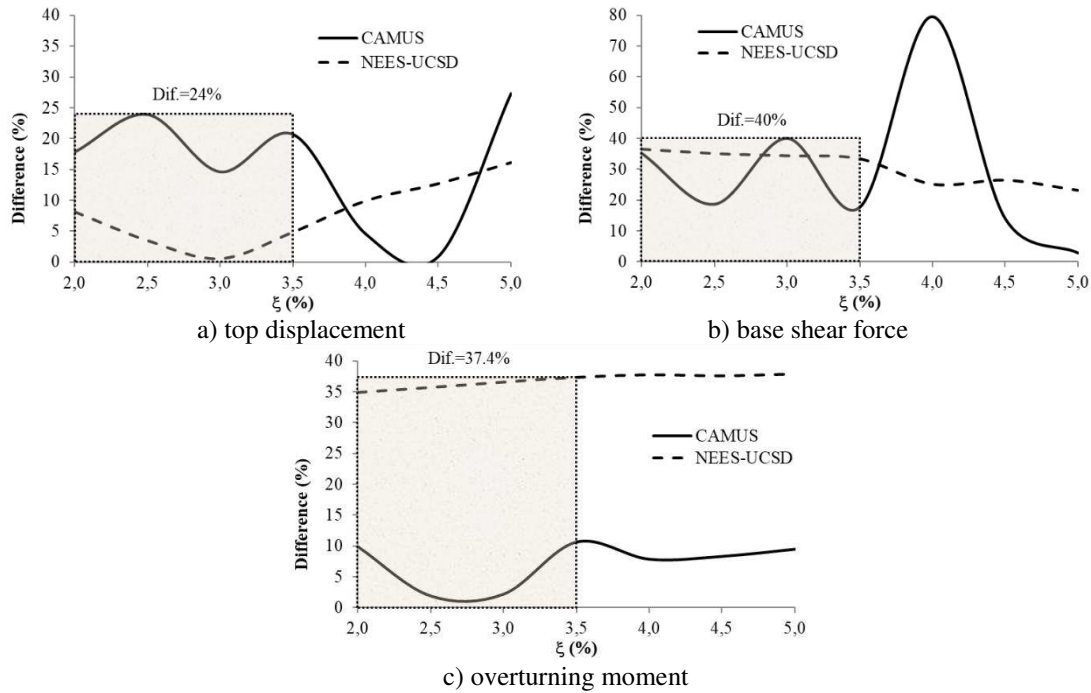


Fig. 23 Comparisons of absolute maximum values obtained by numerical analysis with experimental results of the both shear wall structures for MPD

The differences of the roof displacement, the base shear force and the overturning moment results for SPD with the damping ratios that vary between 2.0% and 3.0% are less than 10.9%, 20.4% and 31.0%, respectively (Fig. 21). The differences of the roof displacement, the base shear force and the overturning moment results for RD with the damping ratios that vary between 2.0% and 3.0% are less than 8.8%, 31.0% and 35.6%, respectively (Fig. 22). However, regarding MPD, the differences of the roof displacement, the base shear force

and the overturning moment results for the damping ratios that vary between 2.0% and 3.5% are less than 24.0%, 40.0% and 37.4%, respectively (Fig.23).

4. Conclusions

In this research, numerical simulation of two RC shear wall structures are conducted to investigate the efficiency of the force-based Fiber Element Method on nonlinear seismic response of the walls. The numerical analysis results are compared with experimental shaking table test results of NEES-UCSD and CAMUS I shear wall structures. Comparisons are carried out regarding the absolute maximum values of the overturning moment, the base shear force, and the roof displacement, and time-history graphs of roof displacements. Dynamic properties of the structures are determined with eigenvalue analysis. Stiffness-proportional damping, mass-proportional damping, and Rayleigh damping types are used for the damping ratios that vary between 2% and 5% in the numerical analyses. Optimum damping ratios are specified for each damping type by using a constant fiber element number (250). To observe the effectiveness of fiber element number on the solutions, the different number of fiber element (70, 80, 90, 100, 500, 750, and 1000) are selected in each cross-section of the structural element. The optimum number of fiber element is defined by considering the (l_f/L_w) ratio. According to comparisons of experimental and numerical analysis results, the following outcomes for the FBFEM method can be expressed as;

- Differences of the roof displacement, the base shear force, and the overturning moment results for stiffness-proportional damping at the damping ratios between 2.0% and 3.0% are less than 10.9%, 20.5%, and 31.0%, respectively.
- In Rayleigh damping type, differences of the roof displacement, the base shear force, and the overturning moment results at the damping ratios between 2.0% and 3.0% are less than 8.8%, 31.0%, and 35.6% respectively.
- Differences of the roof displacement, the base shear force, and the overturning moment results at the damping ratios between 2.0% and 3.5% are less than 24.0%, 40.0%, and 37.4%, respectively for mass-proportional damping.
- The minimum differences of the roof displacement values between numerical and experimental results for the NEES-UCSD and CAMUS I structures are calculated at 3.25% and at 2.49% damping ratios, respectively for the stiffness-proportional damping. For the mass-proportional damping, the least differences for the NEES-UCSD and CAMUS I structures are computed for 3.00% and for 4.52% damping ratios, respectively.
- Provided that the l_f/L_w ratio is smaller than 3% at the optimum damping ratios, the differences between numerical and experimental results in both shear wall structures are computed less than 2.5% for stiffness-proportional and Rayleigh damping types. An inconsistent result is obtained for mass-proportional damping at the optimum damping ratio.
- Stiffness-proportional and Rayleigh damping types give better results than mass-proportional damping. Therefore, these two damping types for the damping ratios that vary between 2-3% are usable in nonlinear seismic analysis of RC shear wall structures with the force-based Fiber Element Method.

DECLARATIONS

Funding

The authors did not receive any funding to conduct this study.

Compliance with ethical standards

Conflicts of interest

All authors have participated in (a) conception and design, or analysis and interpretation of the data; (b) drafting the article or revising it critically for important intellectual content; and (c) approval of the final version.

The authors declare that they have no conflicts of interest relevant to the content of this article.

Availability of data and material

Available upon request

Acknowledgements

This study has been prepared according to Ömer Faruk Osmanlı's M.Sc. thesis results and we would like to thank Mehmet Eren Gülşan and Muhammet Karaton, supervisors of this thesis.

References

- ACI 318-02 (1999), Building code requirements for structural concrete and commentary. American Concrete Institute, Farmington Hills, MI, USA
- Calayir Y, Karaton M (2005) A continuum damage concrete model for earthquake analysis of concrete gravity dam-reservoir systems. *Soil Dyn.&Earth Eng* 25(11): 857–869 <https://doi.org/10.1016/j.soildyn.2005.05.003>
- Celep Z, Kumbasar N (2004) Deprem mühendisliğine giriş ve depreme dayanıklı yapı tasarımı. Beta Dagitim, Istanbul, Turkey
- Correia AA, Virtuoso FBE (2006) Nonlinear Analysis of Space Frames. In: Proceedings of the Third European Conference on Computational Mechanics: Solids, Structures and Coupled Problems in Engineering, Springer, Dordrecht, Lisbon, Portugal, pp 107-107. https://doi.org/10.1007/1-4020-5370-3_107
- Dashti F, Dhakal RP, Pampanin S (2017) Numerical modeling of rectangular reinforced concrete structural walls. *J Struc Eng* 143(6): 04017031. [https://doi.org/10.1061/\(ASCE\)ST.1943-541X.0001729](https://doi.org/10.1061/(ASCE)ST.1943-541X.0001729)
- Feng DC, Ren XD, Li J (2018) Cyclic behavior modeling of reinforced concrete shear walls based on softened damage-plasticity model. *Eng Struc* 166: 363-375. <https://doi.org/10.1016/j.engstruct.2018.03.085>
- Feng DC, Xu J (2018) An efficient fiber beam-column element considering flexure–shear interaction and anchorage bond-slip effect for cyclic analysis of RC structures. *Bull Earthq Eng* 16(11): 5425-5452. <https://doi.org/10.1007/s10518-018-0392-y>
- Fritz WP, Jones NP, Igusa T (2009) Predictive models for the median and variability of building period and damping. *J Struc Eng* 135(5): 576-586. [https://doi.org/10.1061/\(ASCE\)0733-9445\(2009\)135:5\(576\)](https://doi.org/10.1061/(ASCE)0733-9445(2009)135:5(576))
- Gilles D, McClure G (2012) In situ dynamic characteristics of reinforced concrete shear wall buildings. In: Structures Congress 2012, Chicago, Illinois, United States, pp. 2235-2245. <https://doi.org/10.1061/9780784412367.196>
- Huang ST, Huang YS, He A, Tang XL, Chen QJ, Liu X, Cai J (2018) Experimental study on seismic behaviour of an innovative composite shear wall. *Journal of Constructional Steel Research* 148: 165-179. <https://doi.org/10.1016/j.jcsr.2018.05.003>
- Karaton M (2014) Comparisons of elasto fiber and fiber bernoulli-euler reinforced concrete beam-column elements. *Struc Eng& Mech* 51(1): 89–110. <https://doi.org/10.12989/sem.2014.51.1.089>
- Kazaz I, Yakut A, Gülkan P (2006) Numerical simulation of dynamic shear wall tests: A benchmark study. *Comp&Struc* 84(8–9): 549–562. <https://doi.org/10.1016/j.compstruc.2005.11.002>
- Kolozvari K, Tran TA, Orakcal K, Wallace JW (2015) Modeling of cyclic shear-flexure interaction in reinforced

- concrete structural walls. II: Experimental validation. *J Struc Eng* 141(5): 04014136. [https://doi.org/10.1061/\(ASCE\)ST.1943-541X.0001083](https://doi.org/10.1061/(ASCE)ST.1943-541X.0001083)
- Li ZX, Gao Y, Zhao Q (2016) A 3D flexure–shear fiber element for modeling the seismic behavior of reinforced concrete columns. *Eng Struc* 117: 372-383. <https://doi.org/10.1016/j.engstruct.2016.02.054>
- Li G, Yu DH, Li HN (2018) Seismic response analysis of reinforced concrete frames using inelasticity-separated fiber beam-column model. *Earth Eng&Struc Dyn*, 47(5): 1291–1308. <https://doi.org/10.1002/eqe.3018>
- Mander JB, Priestley MJ, Park R (1988) Theoretical stress-strain model for confined concrete. *J Struc Eng* 114(8): 1804–1826. [https://doi.org/10.1061/\(ASCE\)0733-9445\(1988\)114:8\(1804\)](https://doi.org/10.1061/(ASCE)0733-9445(1988)114:8(1804))
- Martinelli L, Martinelli P, Mulas MG (2013) Performance of fiber beam-column elements in the seismic analysis of a lightly reinforced shear wall. *Eng Struc* 49: 345–359 <http://dx.doi.org/10.1016/j.engstruct.2012.11.010>
- Martinelli P (2007) Shaking table tests on rc shear walls: significance of numerical modeling. Dissertation, Politecnico di Milano, Italy
- Martinelli P, Filippou FC (2009) Simulation of the shaking table test of a seven-story shear wall building. *Earth Eng&Struc Dyn* 38(5): 587–607. <https://doi.org/10.1002/eqe.897>
- Menegotto M, Pinto PE (1973) Method of analysis for cyclically loaded RC plane frames including changes in geometry and non-elastic behaviour of elements under combined normal force and bending. In: Proceedings of IABSE symposium on resistance and ultimate deformability of structures acted on by well defined repeated loads, Lisbon, pp 15–22
- Nikolić Ž, Živaljić N, Smoljanović H, Balić I (2017) Numerical modelling of reinforced-concrete structures under seismic loading based on the finite element method with discrete inter-element cracks. *Earth Eng&Struc Dyn*, 46(1): 159-178. <https://doi.org/10.1002/eqe.2780>
- Orakcal K, Wallace JW, Conte JP (2004) Flexural modeling of reinforced concrete walls-model attributes. *Struc J*, 101(5): 688-698. <https://doi.org/10.14359/13391>
- Peterman KD, Stehman MJ, Madsen RL, Buonopane SG, Nakata N, Schafer BW (2016) Experimental seismic response of a full-scale cold-formed steel-framed building. II: Subsystem-level response. *J Struc Eng*, 142(12): 04016128. [https://doi.org/10.1061/\(ASCE\)ST.1943-541X.0001578](https://doi.org/10.1061/(ASCE)ST.1943-541X.0001578)
- Rong XL, Zheng SS, Zhang YX, Zhang XY, Dong LG (2020) Experimental study on the seismic behavior of RC shear walls after freeze-thaw damage. *Eng Struc*, 206: 110101. <https://doi.org/10.1016/j.engstruct.2019.110101>
- Seismosoft (2016), SeismoStruct 2016 – A computer program for static and dynamic nonlinear analysis of framed structures. Available from <http://www.seismosoft.com>
- Shen D, Yang Q, Jiao Y, Cui Z, Zhang J (2017) Experimental investigations on reinforced concrete shear walls strengthened with basalt fiber-reinforced polymers under cyclic load. *Constr Build Mater*, 136, 217-229. <https://doi.org/10.1016/j.conbuildmat.2016.12.102>
- Taucer FF, Spacone E, Filippou FC (1991) A fiber beam-column element for seismic response analysis of reinforced concrete structures, Report No. UCB/EERC-91/17, Earthquake Engineering Research Center, College of Engineering, University of California, Berkeley
- Vásquez JA, Juan C, de la L, Matías H (2016) A regularized fiber element model for reinforced concrete shear walls. *Earth Eng&Struc Dyn* 45: 2063–2083. <https://doi.org/10.1002/eqe.2731>
- Wang W, Wang Y, Lu Z (2018) Experimental study on seismic behavior of steel plate reinforced concrete composite shear wall. *Eng Struc* 160: 281-292. <https://doi.org/10.1016/j.engstruct.2018.01.050>
- Zhang S, Cheng M, Wang J, Wu JY (2020) Modeling the hysteretic responses of RC shear walls under cyclic loading by an energy-based plastic-damage model for concrete. *Int J Damage Mech* 29(1): 184-200. <https://doi.org/10.1177/1056789519889103>

Figures

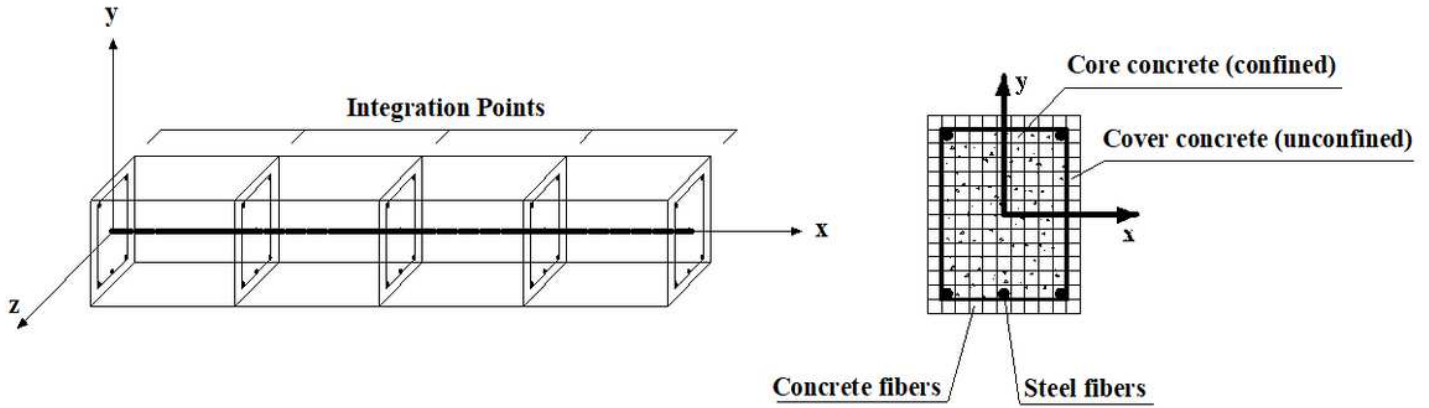


Figure 1

The fiber beam-column element and discretization of the cross-section (Seismosoft, 2016)

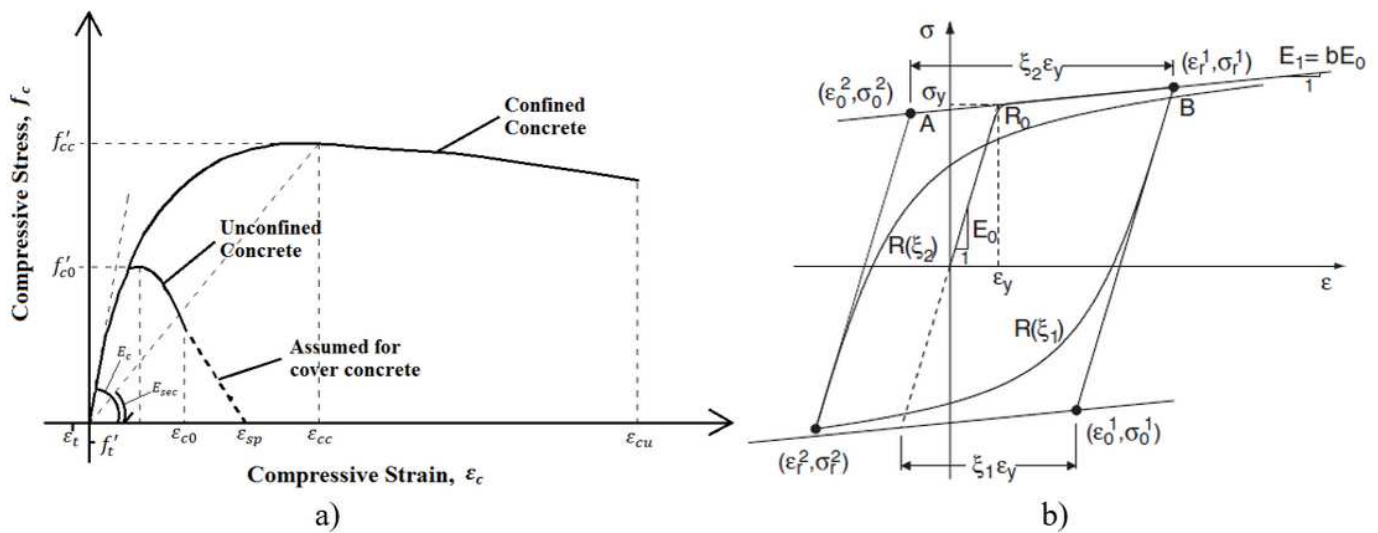


Figure 2

a) Mander-Priestley-Park concrete model (Mander et al., 1988) and b) Modified Menegotto and Pinto steel model (Koložvari et al., 2015).

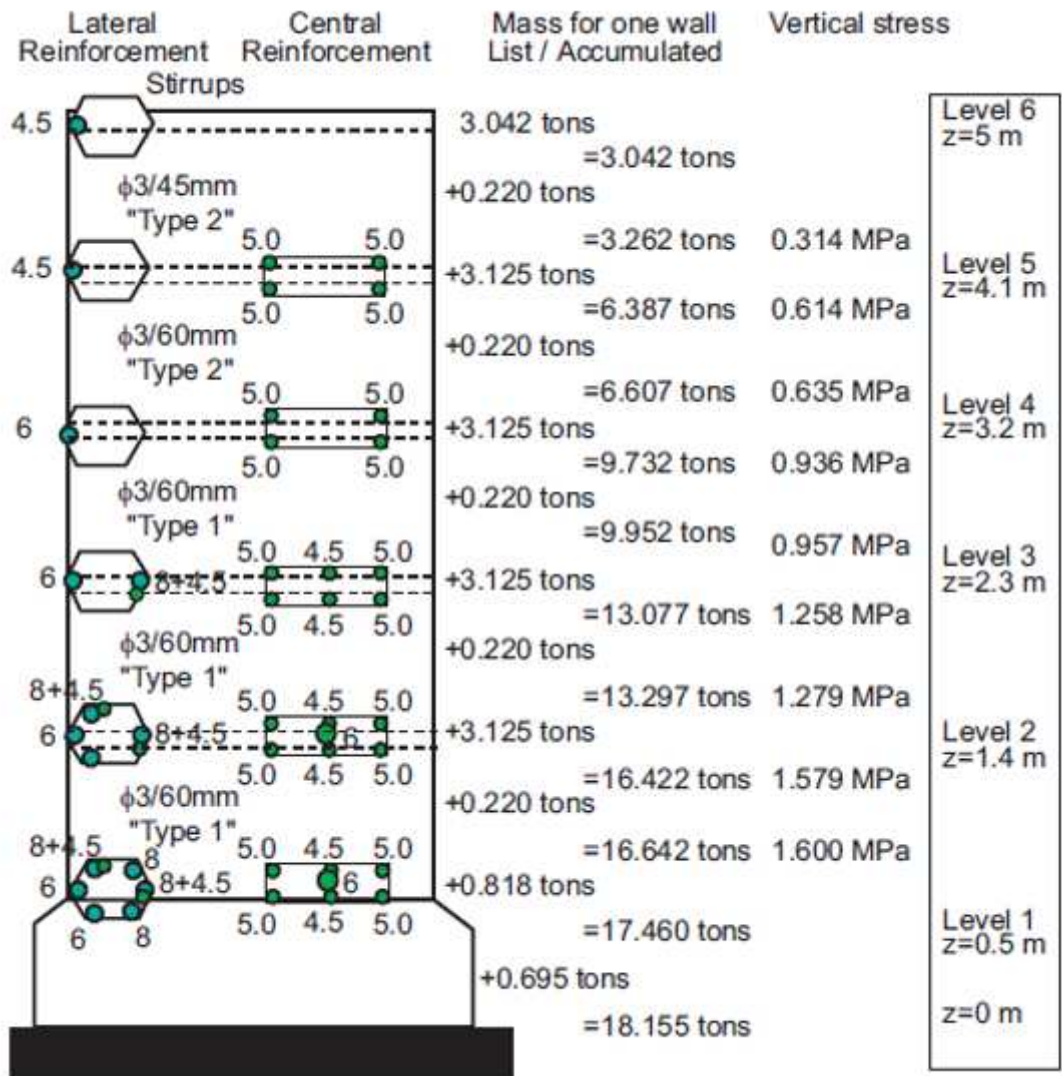


Figure 3

Steel reinforcement and mass details for one wall of the CAMUS I structure (Martinelli, 2007)

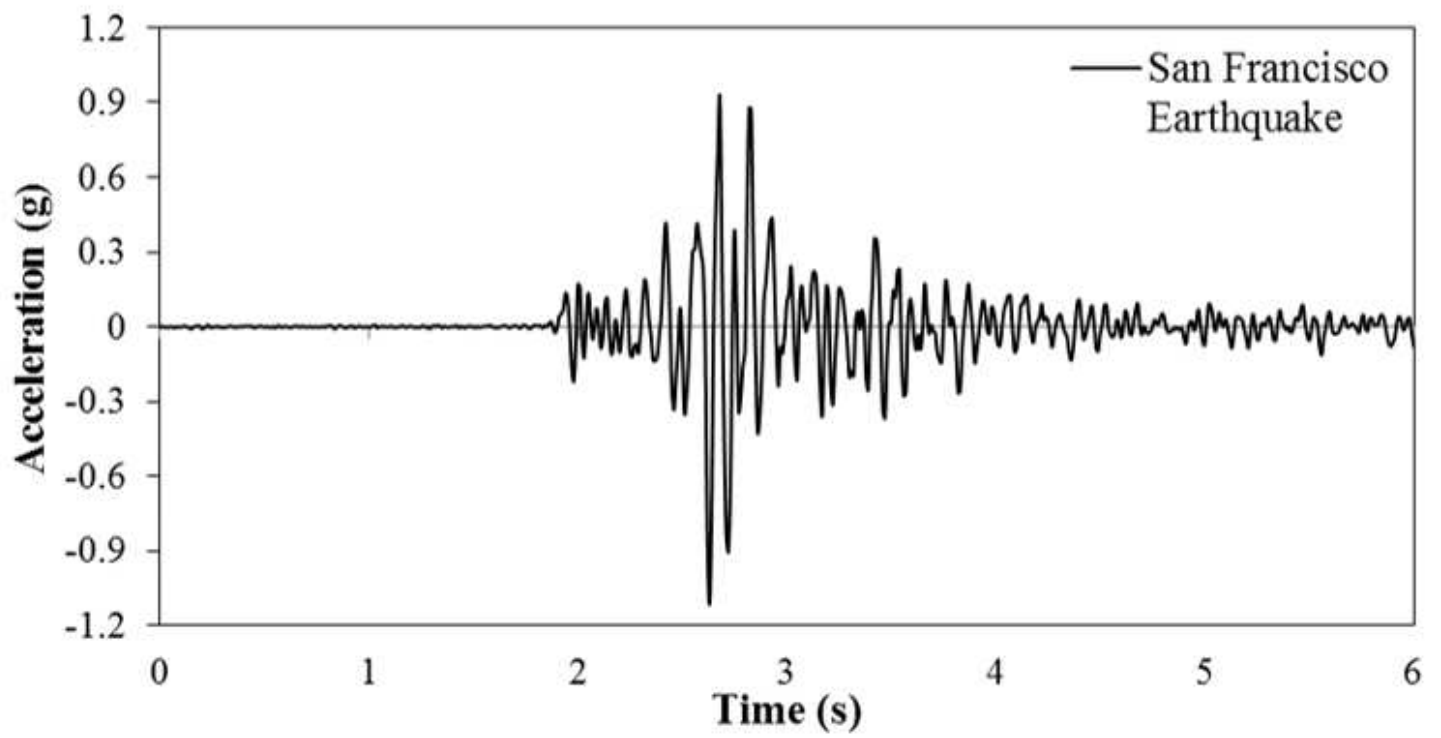


Figure 4

The scaled 1957 San Francisco earthquake loading (Kazaz et al., 2006)

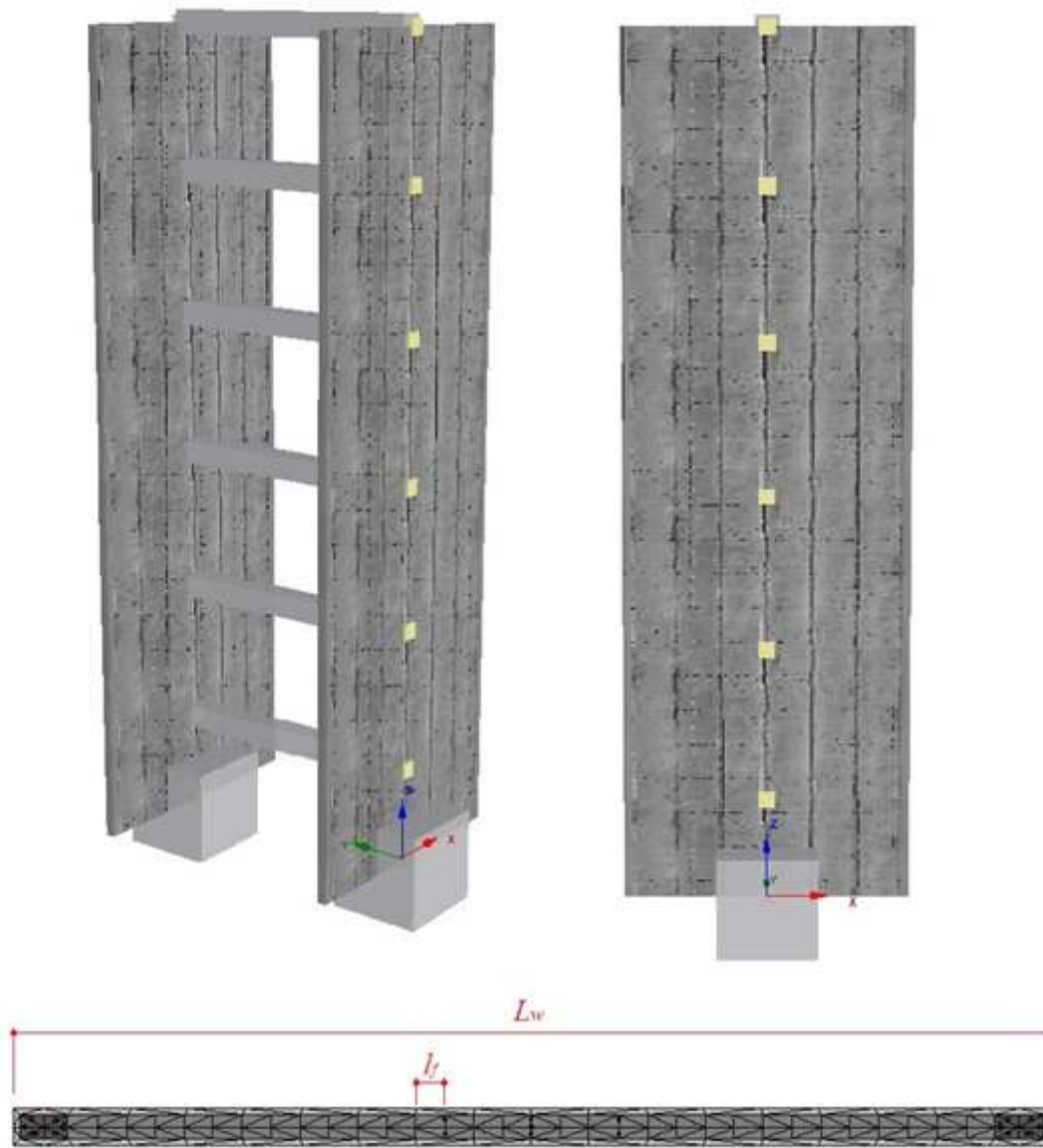


Figure 5

3D view of the CAMUS I structure model and meshing of the shear wall

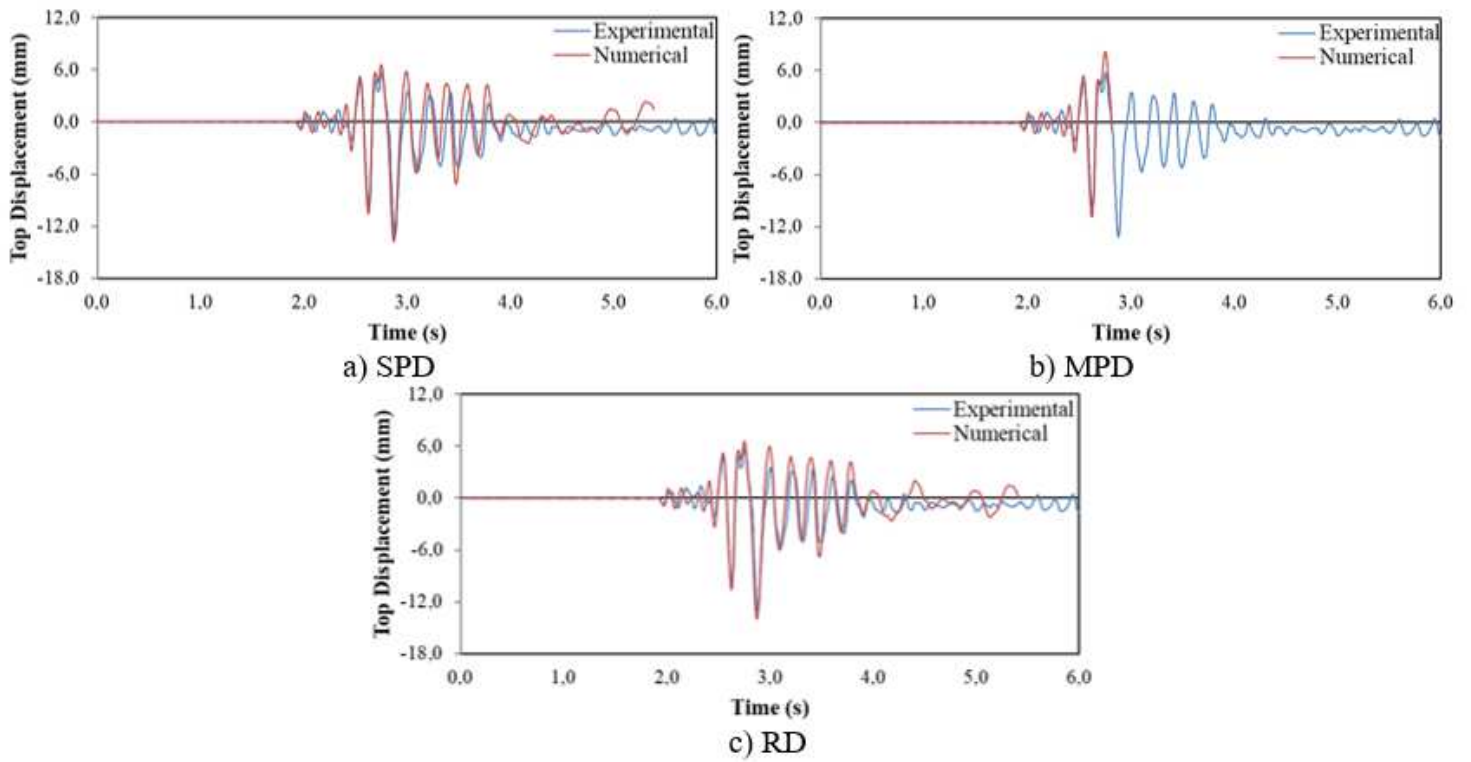


Figure 6

Top displacement responses of the CAMUS I for the damping ratio of 2%

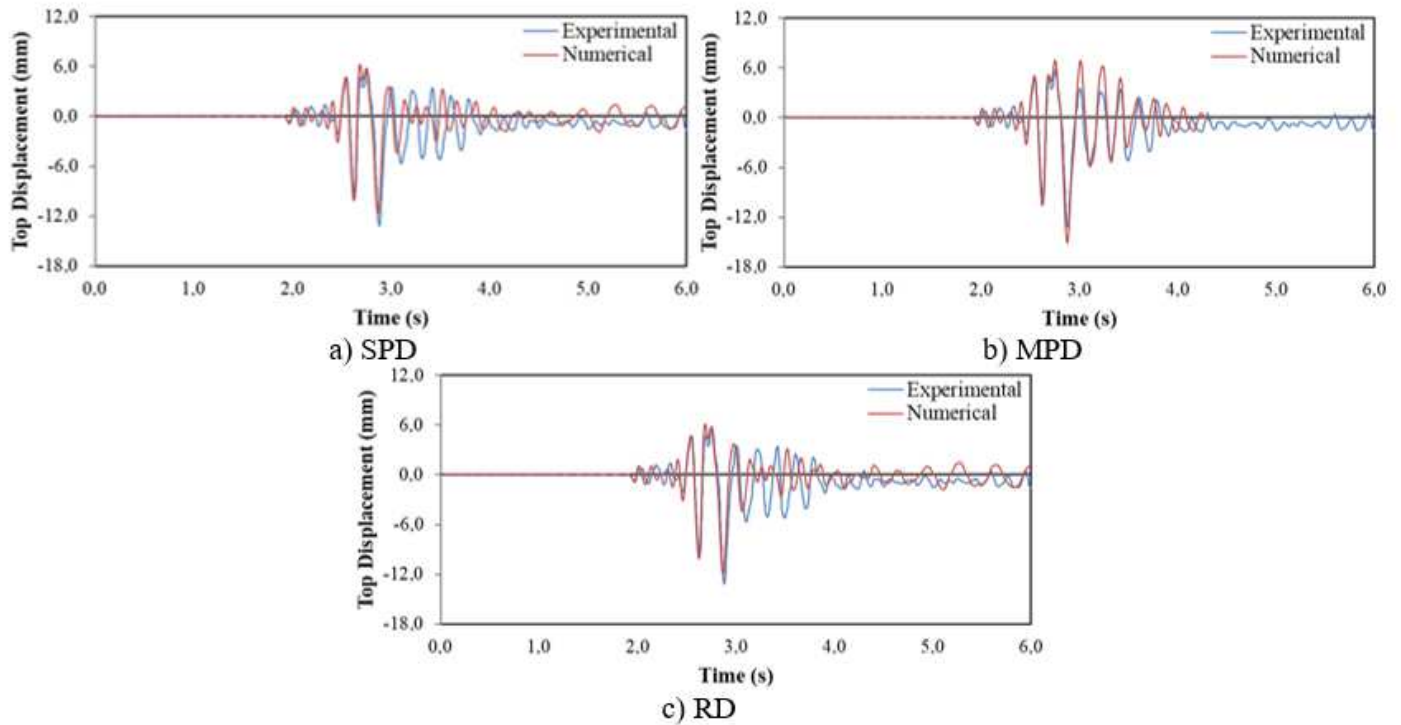


Figure 7

Top displacement responses of the CAMUS I for the damping ratio of 3%

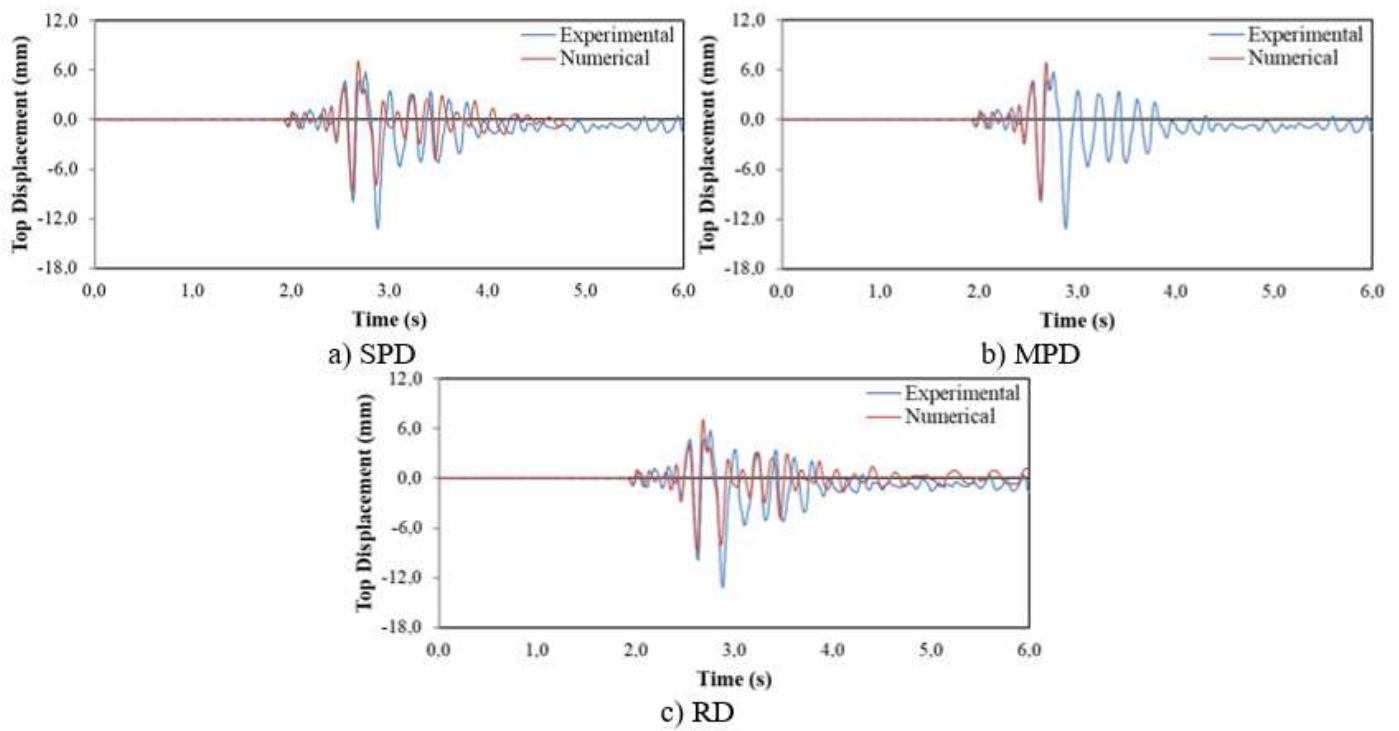


Figure 8

Top displacement responses of the CAMUS I for the damping ratio of 5%

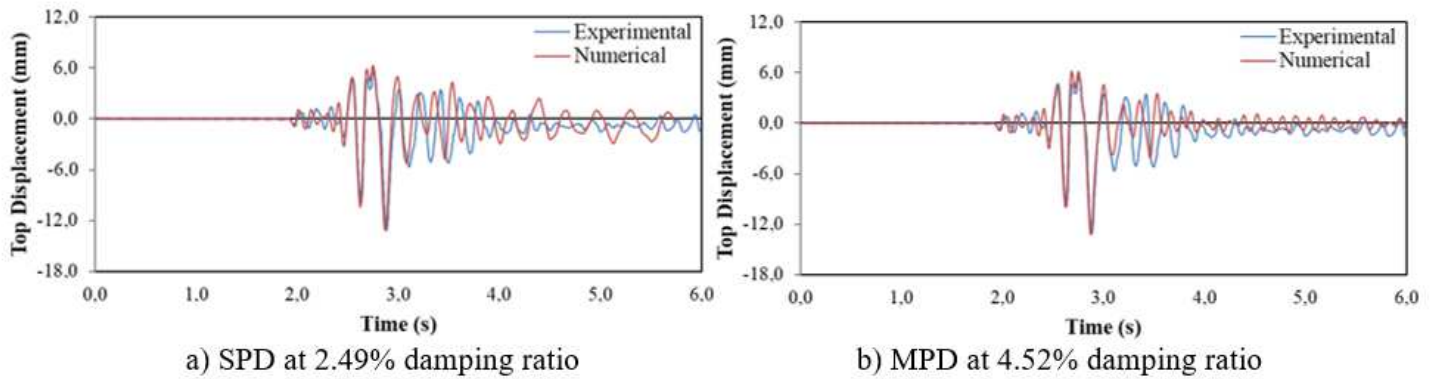


Figure 9

Top displacement responses of the CAMUS I for SPD and MPD types at the optimum damping ratios

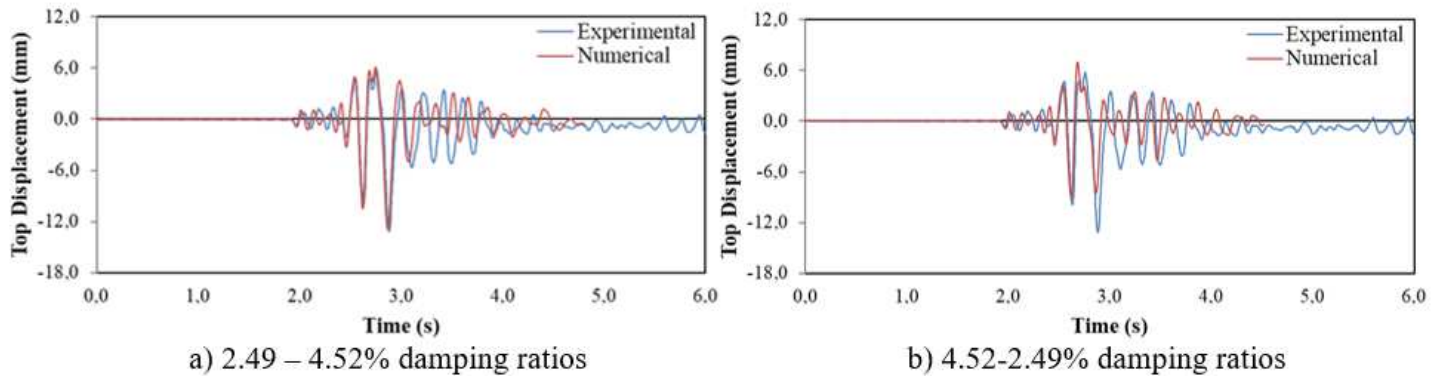


Figure 10

Top displacement responses of the CAMUS I for RD at the optimum damping ratios of the first two effective modes

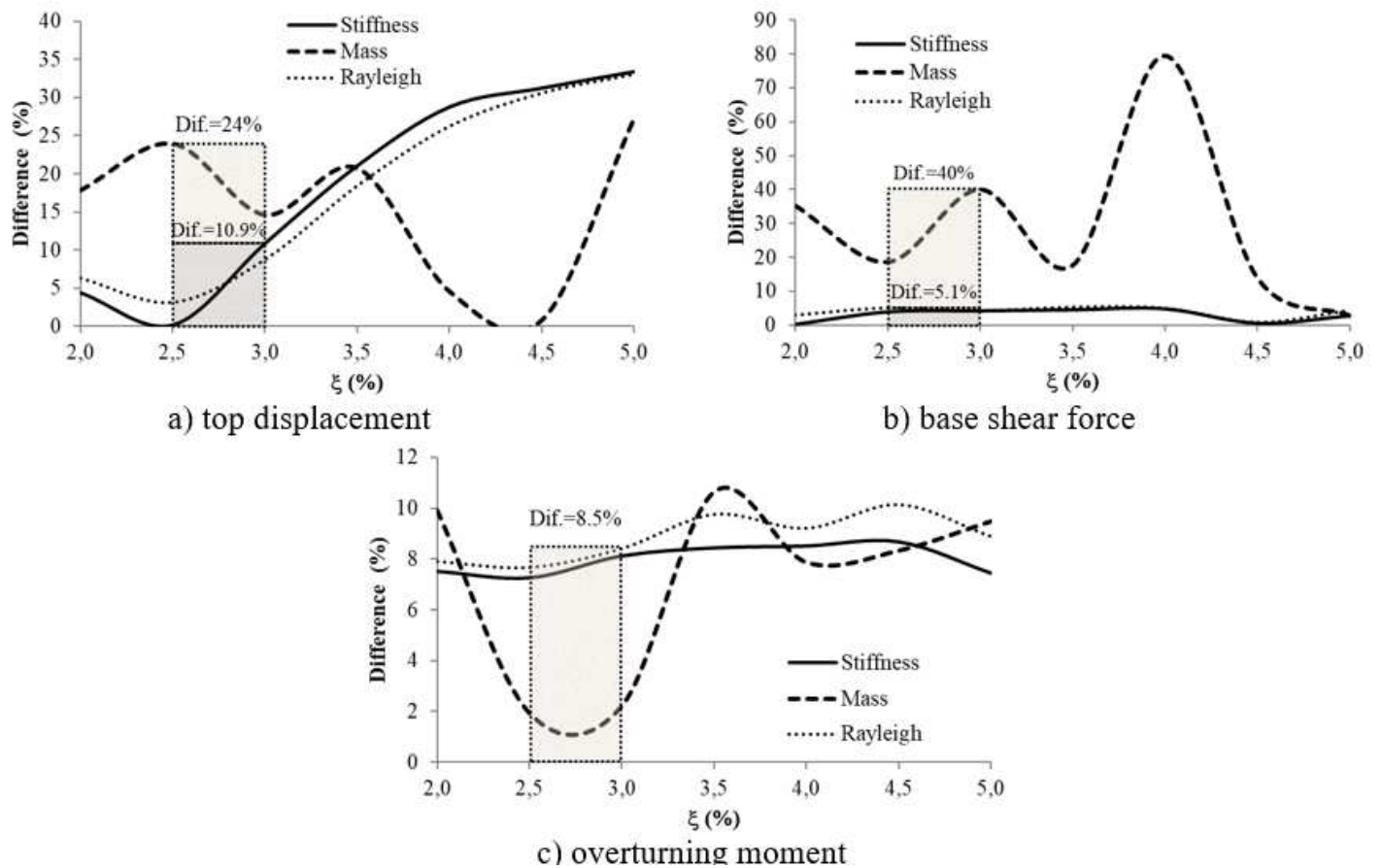


Figure 11

Comparisons of absolute maximum values obtained by numerical analysis with experimental results of the CAMUS I structure for various damping types

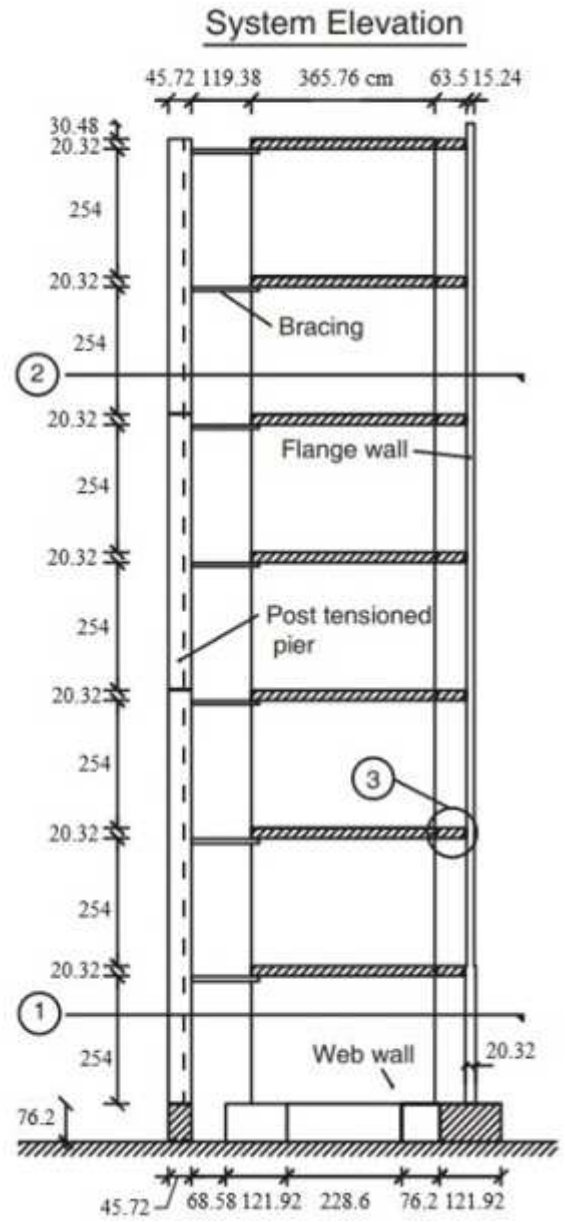


Figure 12

NEES-UCSD structure (Martinelli, 2007)

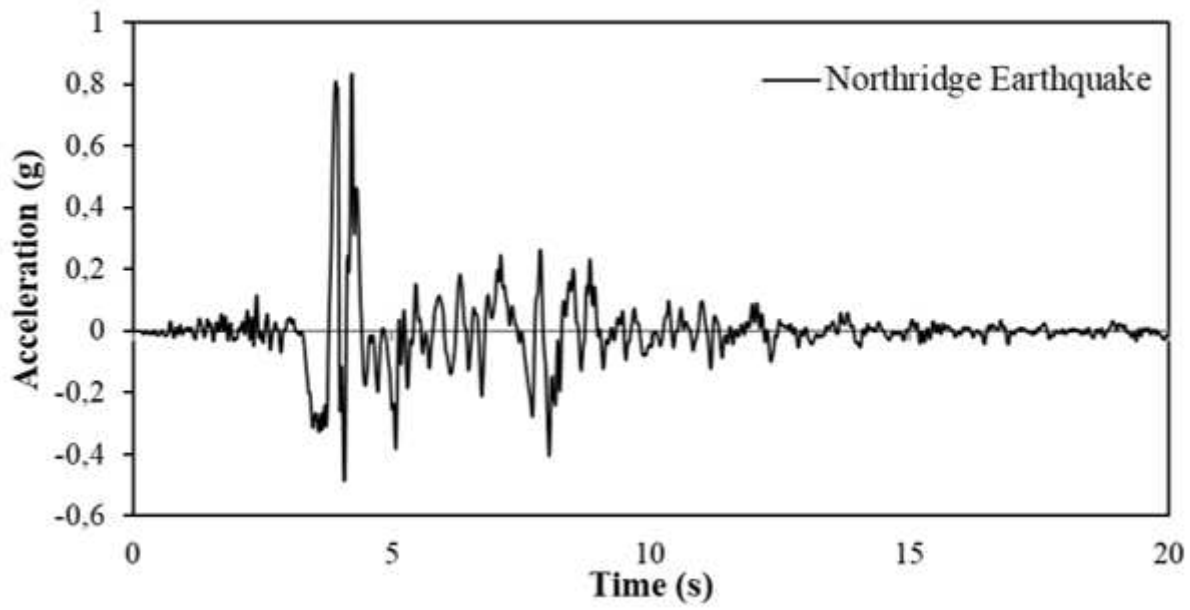


Figure 13

The acceleration record of the 1994 Northridge earthquake (Seismosoft, 2016)

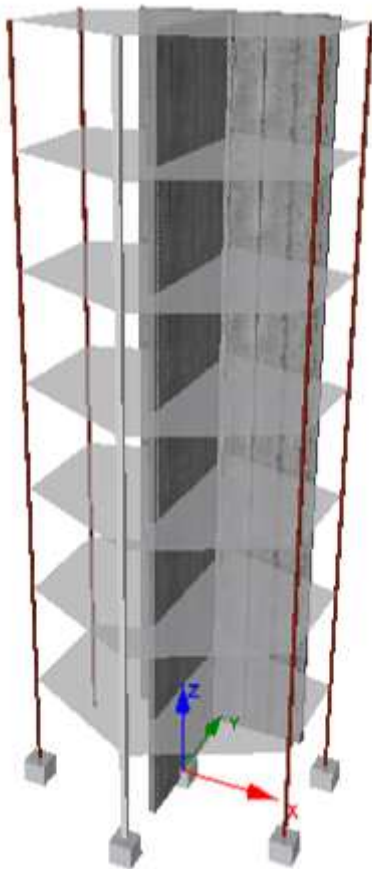


Figure 14

3D view of the NEES-UCSD structure model

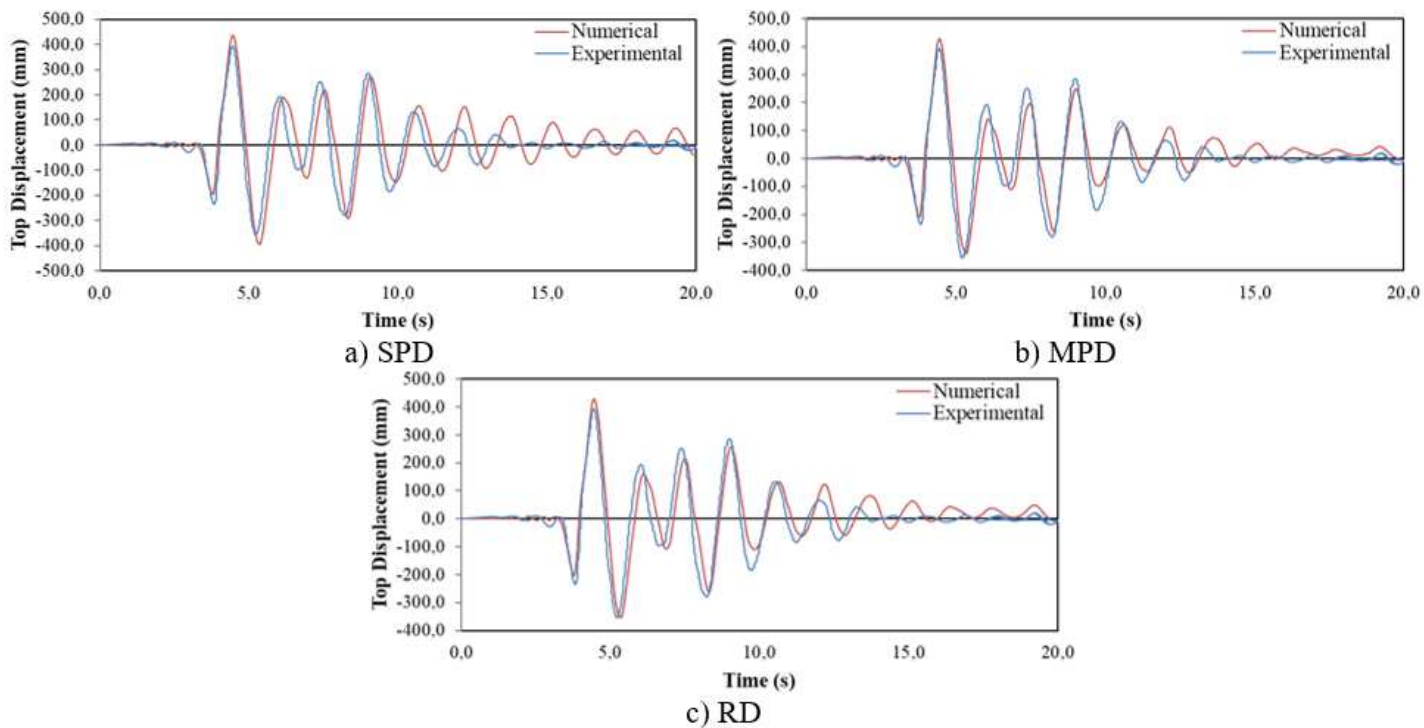


Figure 15

Top displacement responses of the CAMUS I for the damping ratio of 2%

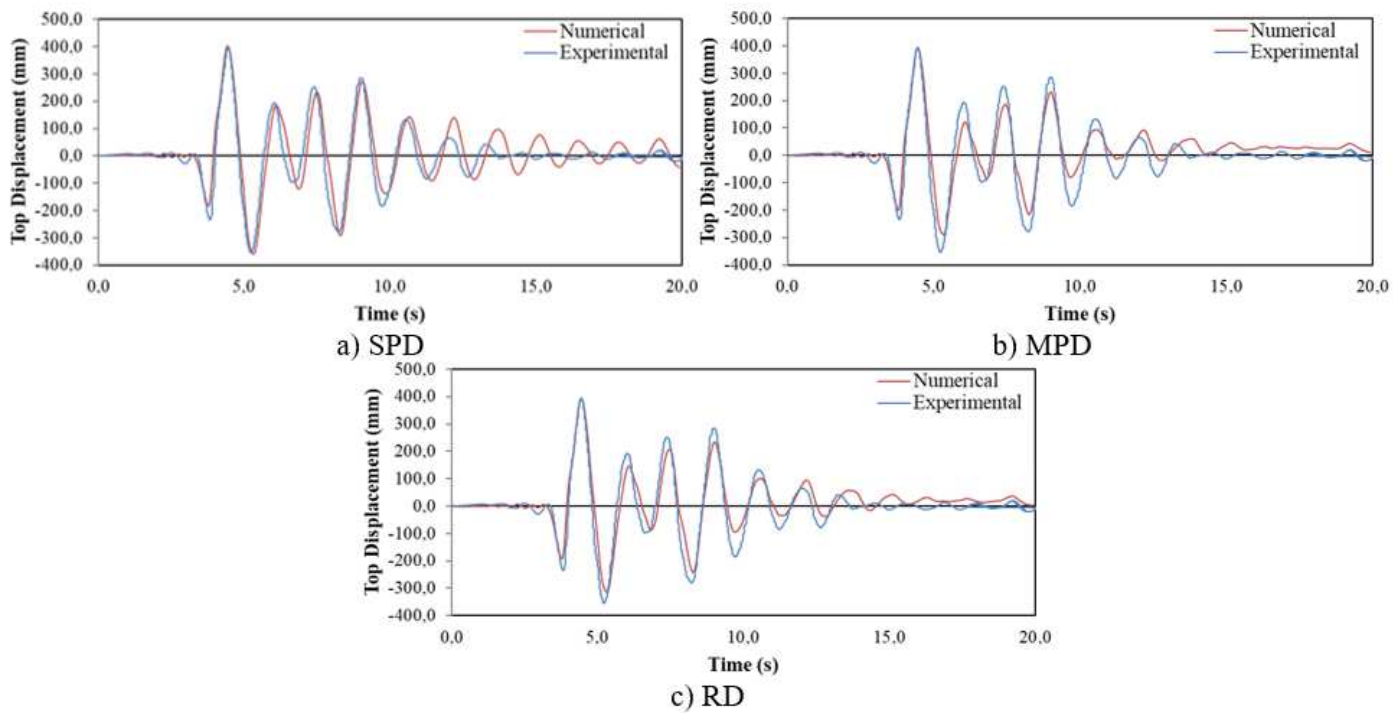


Figure 16

Top displacement responses of the CAMUS I for the damping ratio of 3%

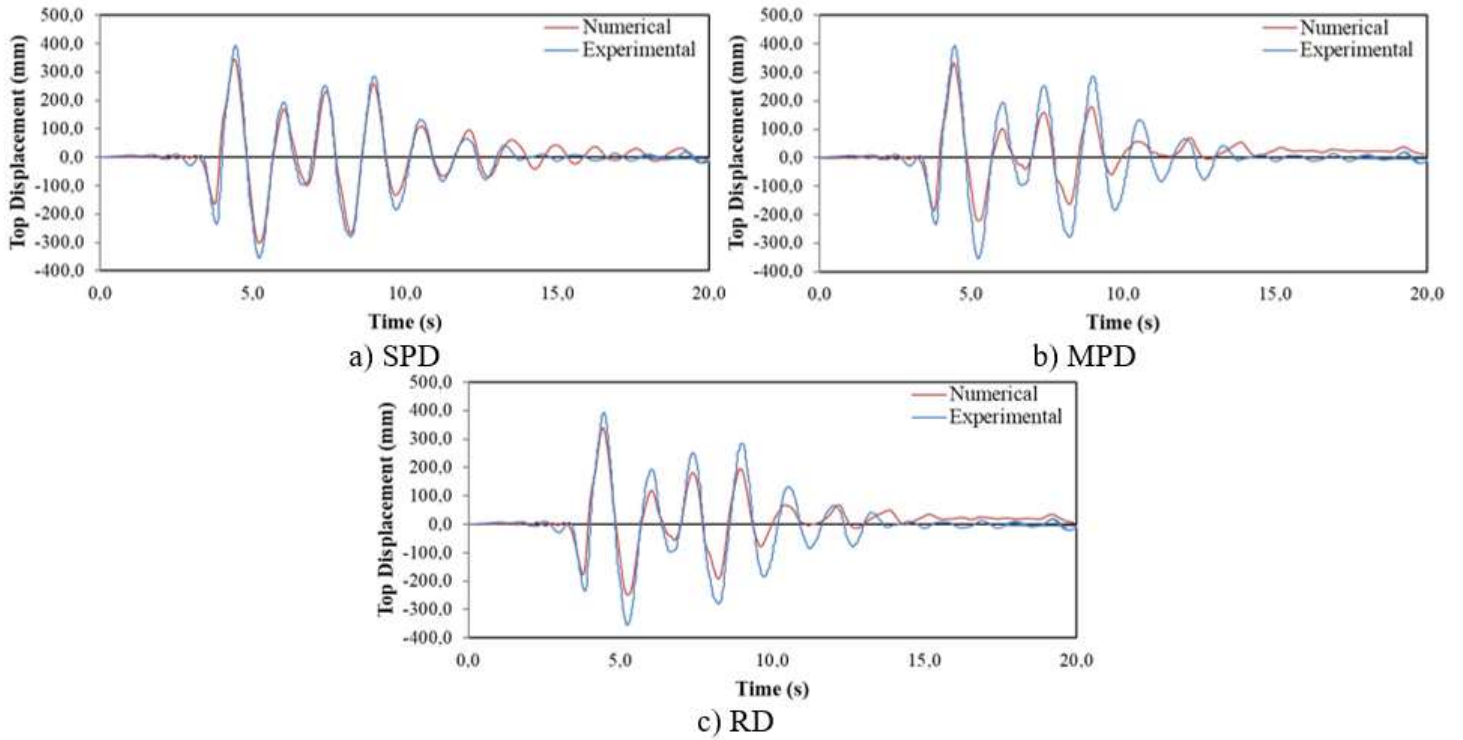


Figure 17

Top displacement responses of the CAMUS I for the damping ratio of 5%

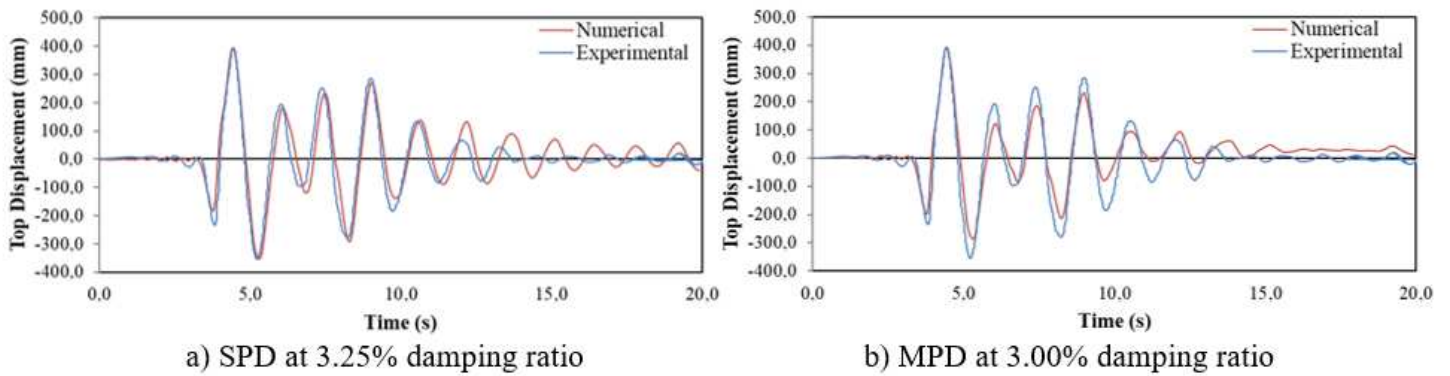


Figure 18

Top displacement responses of the NEES-UCSD for SPD and MPD types at optimum damping ratios

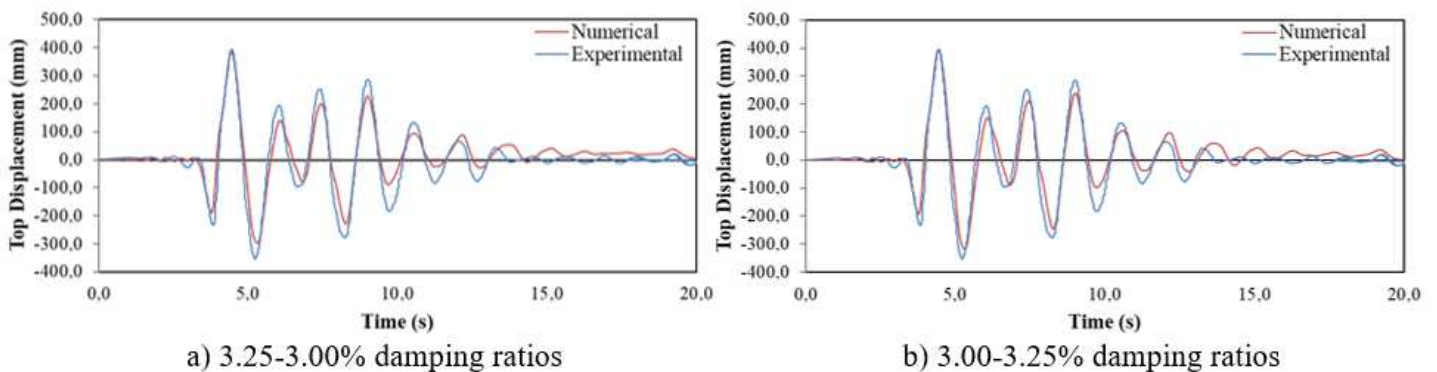


Figure 19

Top displacement responses of the NEES-UCSD for RD type at the optimum damping ratios of the first two effective modes

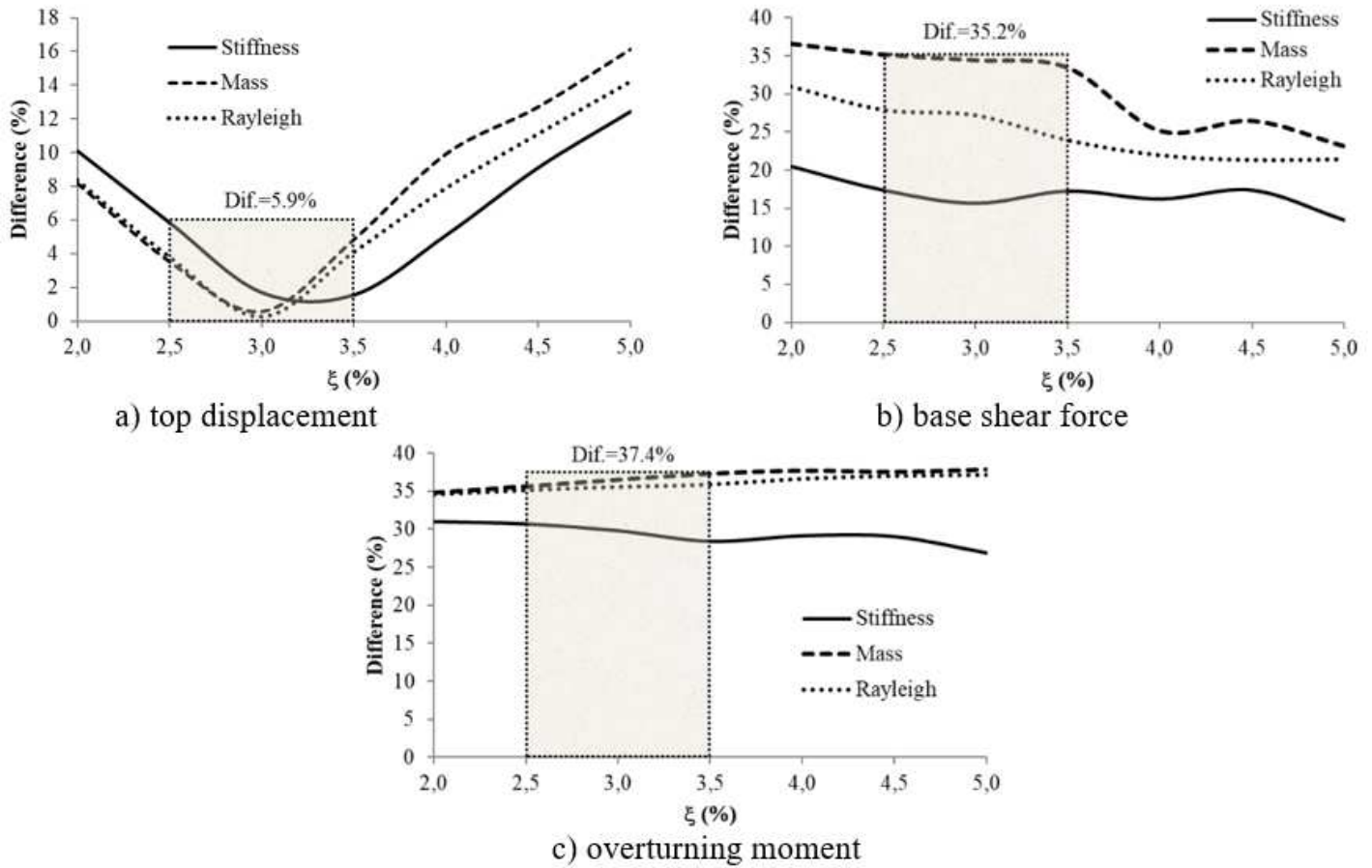
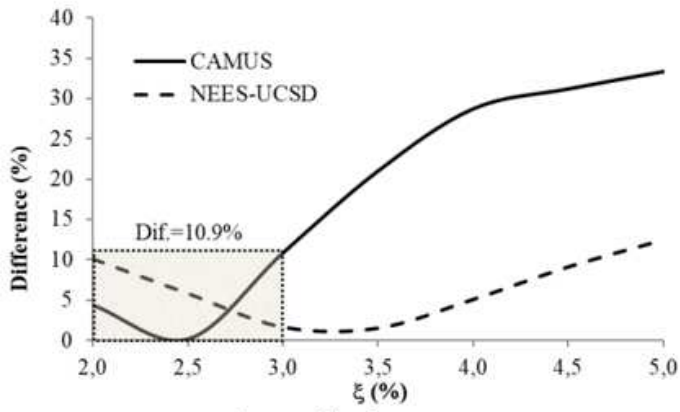
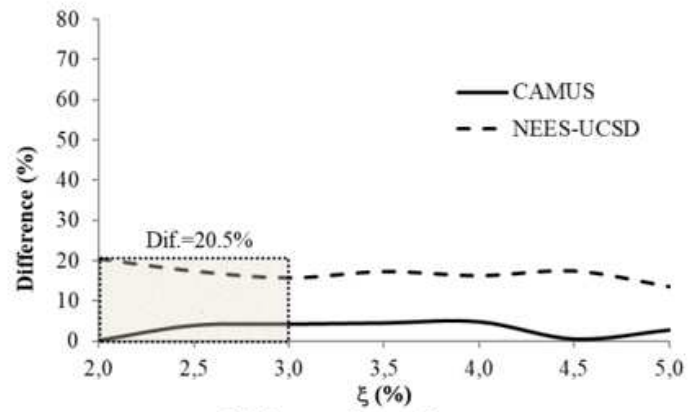


Figure 20

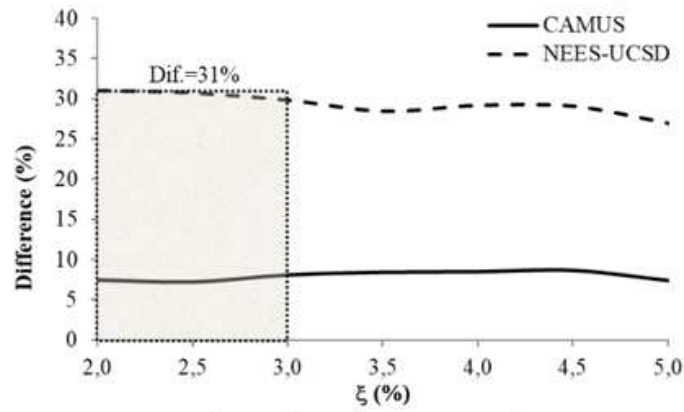
Comparisons of absolute maximum values obtained by numerical analysis with experimental results of the NEES-UCSD structure for various damping types



a) top displacement



b) base shear force



c) overturning moment

Figure 21

Comparisons of absolute maximum values obtained by numerical analysis with experimental results of the both shear wall structures for SPD

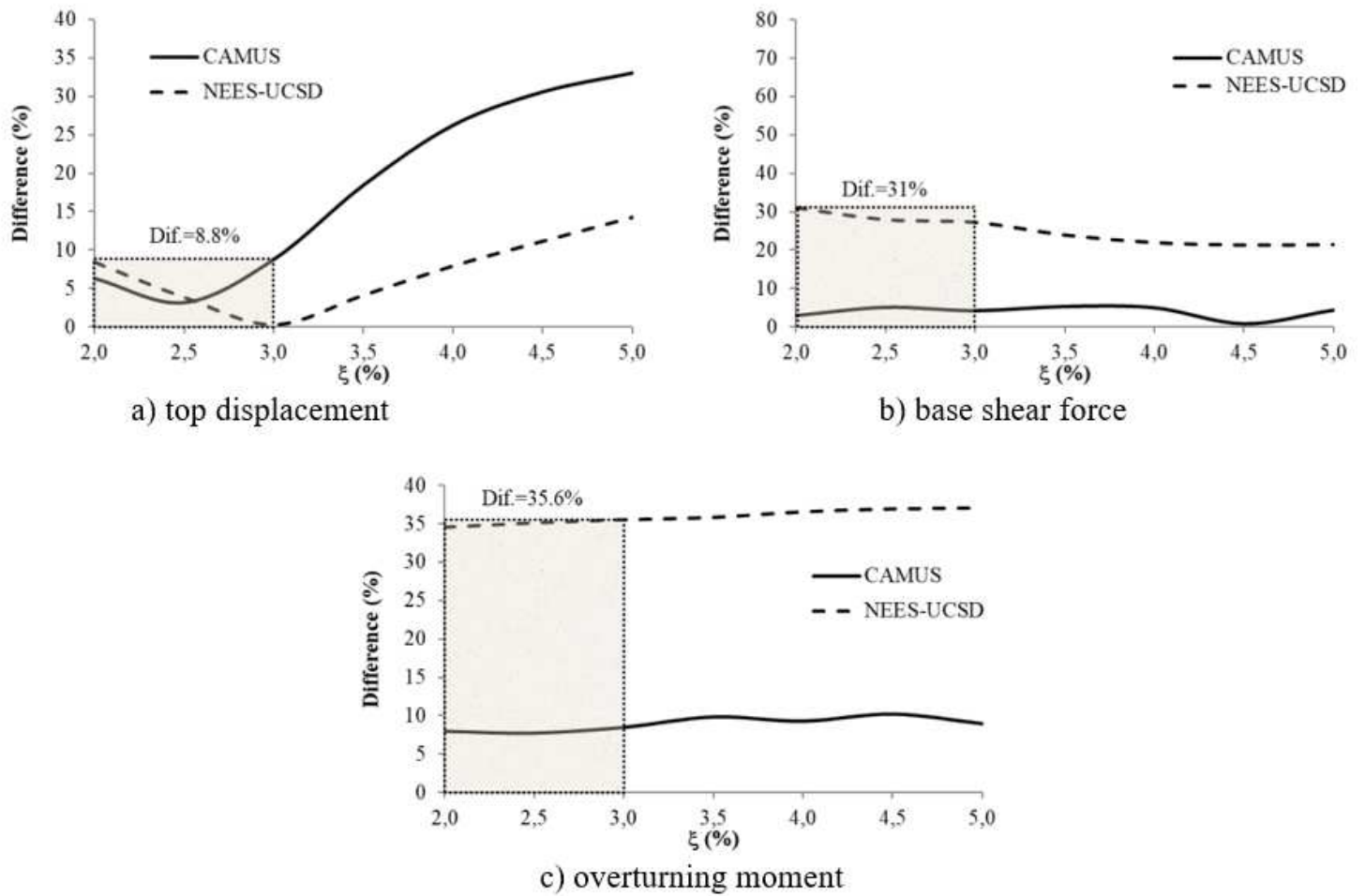
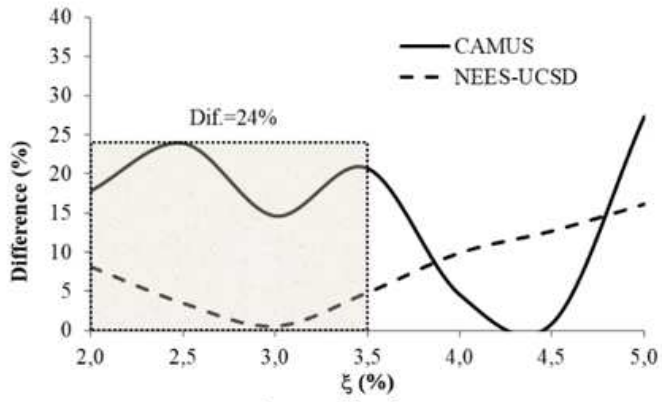
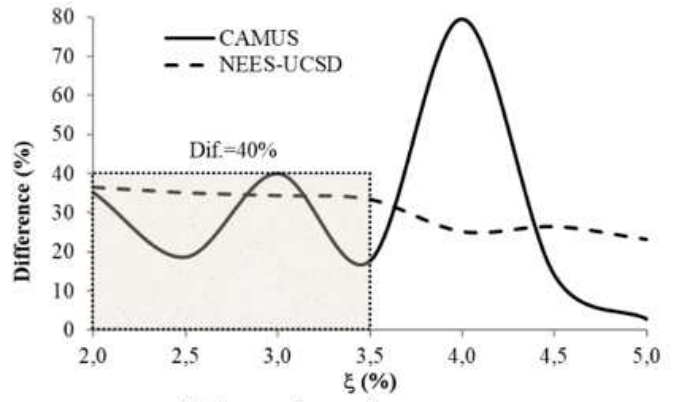


Figure 22

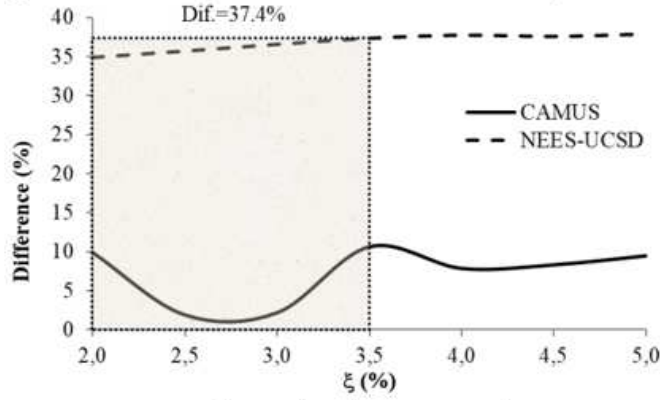
Comparisons of absolute maximum values obtained by numerical analysis with experimental results of the both shear wall structures for RD



a) top displacement



b) base shear force



c) overturning moment

Figure 23

Comparisons of absolute maximum values obtained by numerical analysis with experimental results of the both shear wall structures for MPD